

Efficient quantum-classical method for computing thermal rate constant of recombination: Application to ozone formation

Mikhail V. Ivanov and Dmitri Babikov

Citation: *J. Chem. Phys.* **136**, 184304 (2012); doi: 10.1063/1.4711760

View online: <http://dx.doi.org/10.1063/1.4711760>

View Table of Contents: <http://jcp.aip.org/resource/1/JCPSA6/v136/i18>

Published by the [American Institute of Physics](#).

Additional information on *J. Chem. Phys.*

Journal Homepage: <http://jcp.aip.org/>

Journal Information: http://jcp.aip.org/about/about_the_journal

Top downloads: http://jcp.aip.org/features/most_downloaded

Information for Authors: <http://jcp.aip.org/authors>

ADVERTISEMENT



AIPAdvances

Special Topic Section:
PHYSICS OF CANCER

Why cancer? Why physics? [View Articles Now](#)

Efficient quantum-classical method for computing thermal rate constant of recombination: Application to ozone formation

Mikhail V. Ivanov and Dmitri Babikov^{a)}

Chemistry Department, Wehr Chemistry Building, Marquette University, Milwaukee, Wisconsin 53201-1881, USA

(Received 4 November 2011; accepted 18 April 2012; published online 10 May 2012)

Efficient method is proposed for computing thermal rate constant of recombination reaction that proceeds according to the energy transfer mechanism, when an energized molecule is formed from reactants first, and is stabilized later by collision with quencher. The mixed quantum-classical theory for the collisional energy transfer and the ro-vibrational energy flow [M. Ivanov and D. Babikov, *J. Chem. Phys.* **134**, 144107 (2011)] is employed to treat the dynamics of molecule + quencher collision. Efficiency is achieved by sampling simultaneously (i) the thermal collision energy, (ii) the impact parameter, and (iii) the incident direction of quencher, as well as (iv) the rotational state of energized molecule. This approach is applied to calculate third-order rate constant of the recombination reaction that forms the $^{16}\text{O}^{18}\text{O}^{16}\text{O}$ isotopomer of ozone. Comparison of the predicted rate vs. experimental result is presented. © 2012 American Institute of Physics. [<http://dx.doi.org/10.1063/1.4711760>]

I. INTRODUCTION

Our general purpose is to develop an affordable practical method for theoretical treatment of dynamics in recombination reactions that follow the energy transfer mechanism.¹⁻⁵



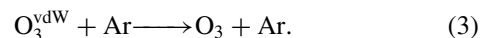
Here $\text{A} + \text{BC}$ represent reactants, ABC is a stable final product of recombination, while ABC^* represents a metastable reaction intermediate excited ro-vibrationally above the dissociation threshold (a scattering resonance). The quencher M serves to remove energy from ABC^* and can be an atom or molecule of the bath gas. In the low pressure regime, when the frequency (or efficiency) of the deactivating collisions in the step (2) is low, one can assume that pre-equilibrium is achieved in the step (1). Thus, in the treatment of recombination kinetics, the equilibrium constant K_{eq} for step (1) and the second order rate coefficient of stabilization k_{stab} for step (2) both play essential roles.

The theoretical treatment of the recombination reactions (1) and (2) is a very challenging task. Note that even in the simplest case, when the quencher M is an inert atom (such as Ar), the overall process involves four nuclei. The full quantum treatment of tetra-atomic reactions still represents a formidable challenge to the chemical physics community and, so far, has been carried out for very few systems.⁶⁻¹¹ Thus, it would be desirable to have an alternative to the full quantum method.

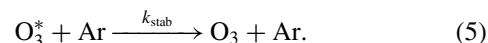
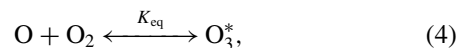
In a recent paper¹² we proposed a mixed quantum-classical method for treatment of the collisional energy trans-

fer and the ro-vibrational energy flow in the step (2) of a recombination reaction. One approximation of our theory is separation of all degrees of freedom in the system onto the classical and quantum parts. Namely, we use the time-dependent quantum mechanics (the wave packet method) to treat the internal vibrational motion of the energized molecule ABC^* , while the rotational motion of ABC^* and the collisional $\text{ABC}^* + \text{M}$ motion are treated with classical trajectories. The rotation-vibration couplings in ABC^* are included in an adiabatic manner.¹³⁻¹⁵ The energy is exchanged between translational, rotational and vibrational degrees of freedom, while the total energy in the system is conserved.

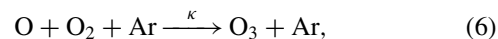
Our method captures major quantum effects associated with vibrational motion of ABC^* (i.e., zero-point energy, quantization of states, tunneling, scattering resonances), while the advantage is taken of the quasi-classical regime usually valid for rotational and translational degrees of freedom. In another recent paper¹⁶ we applied this approach to obtain detailed insight into stabilization of the van der Waals (vdW) states of ozone molecule in a collision with Ar atom:



Here, in the third paper of this series, we apply our mixed quantum-classical approach to treat the deactivation of scattering resonances O_3^* in the ozone forming reaction:



The overall ozone forming reaction



has been intensively studied in the past from different perspectives,¹⁷⁻³² but very little is actually known about the collisional energy transfer step, the process (5). The first study

^{a)} Author to whom correspondence should be addressed. Electronic mail: dmitri.babikov@marquette.edu.

by Charlo and Clary^{33,34} has employed, within the time independent coupled-channel formalism, a frozen-bending approximation for O_3^* and a sudden-collision assumption for $O_3^* + Ar$. While the reduced dimensionality approximation itself is a viable approach, the work of Clary suffered, from our point of view, from a very unfortunate combination of the multi-channel nature of the process and the Jacobi coordinates used to freeze the bending angle in O_3^* . The next study by Xie and Bowman³⁵ has offered a considerable improvement by implementing the full-dimensional treatment of O_3^* . However, their calculations have been carried out for very few (just three) combinations of impact parameter of Ar and orientation of O_3^* . The next contribution was a classical-trajectory study by Ivanov and Schinke.^{36,37} Finally, an approximate quantum treatment was proposed^{38,39} by the same group. Similar to the methods of Clary and Bowman, the quantum method of Ivanov and Schinke was also based on the coupled-channel formalism and the sudden-collision assumption. Their calculations converged with respect to the number of partial waves, but their basis set included just the bound states of non-rotating O_3 (no scattering resonances). Unfortunately, such results cannot be reliable near threshold for dissociation/recombination which, in fact, is the most important energy range in this problem. Also, Ivanov and Schinke have simplified their model considerably by artificially removing the long range van der Waals wells from the entrance/exit channels of O_3 , keeping only the short-range part of the potential energy surface.

The previous paragraph has been given not to criticize the excellent earlier work, but in order to emphasize the complexity of the problem. We hope to overcome some of the difficulties encountered earlier by employing the quantum-classical approach,^{12,16} which has a number of advantages. First of all, our method allows avoiding the sudden approximation and treating the dynamics of $O_3^* + Ar$ scattering in a time-dependent way (classically). This is important, since a typical $O_3^* + Ar$ collision is rather adiabatic than sudden. Second, we do actually treat the rotation of O_3^* , including a broad range of $J > 0$ states, and determine its rotational excitation in collisions with Ar (also classically). These classical approximations are justified because, in this reaction, we do not expect any quantum effects due to scattering of heavy Ar or due to rotation of heavy O_3^* . Nevertheless, within the quantum-classical framework, we are able to produce cross sections for transitions between quantized vibrational states of O_3^* (quantum mechanically). The scattering resonances of O_3^* are accessible, as well as transitions into the long-range vdW well and into the continuum states, followed by dissociation. Large-amplitude vibrational motion is described numerically using the wave-packet technique. Finally, the accurate global PES of ozone¹⁹ is used.

In the current implementation, similar to Clary, we still use the reduced dimensionality approximation for the bending of O_3^* , but it is a different one. We treat the bending motion adiabatically using the bond-angle coordinates. This approach preserves the most important features of the complicated ozone PES and keeps it symmetric even in the reduced dimensionality.^{12,16,24} The frozen bending approximation of Clary would be more appropriate at high energies, while our

adiabatic treatment of bending is more appropriate at energies near threshold, specific to the ozone forming reaction.

We should admit, however, that, regardless of particular implementation, the reduced dimensionality approximations always lead to significant reduction of the number of quantized vibrational states of the system. In particular, in the adiabatic bending model employed here, all the excited bending states are missing, leading to reduction of the number of states in O_3 roughly by a factor of seven. In order to compensate for this reduction, we treat the bending motion statistically and introduce, into the formalism of the recombination kinetics, the bending partition function Q_{bend} (see Sec. II). In a sense, this restores the number of scattering resonances O_3^* that receive population from $O + O_2$ collisions and could serve as *initial* states in the $O_3^* + Ar$ collision events. This correction, however, may not be sufficient, because the missing bending states could also serve as *final* states in the $O_3^* + Ar$ collisions, which might create additional pathways for the vibrational energy relaxation. This effect is expected to be important but is impossible to estimate in a simple way (e.g., statistically). The only way to characterize the role of bending states is to carry out the full-dimensional stabilization calculations, which may be possible in the future but is clearly beyond the scope of this paper. In this regard, the numerical value of the recombination rate coefficient κ calculated here is not expected to be particularly accurate. An agreement with experiment within the order of magnitude, which could still provide a semi-quantitative insight, is a reasonable expectation.

So, can we learn anything useful from the dimensionally reduced model? The answer is – definitely yes and a lot, because at this time very little is known about the stabilization step of the ozone forming reaction. Although several papers have been published on this topic^{33–35,38,39} we were not able to find in the literature a single datum on cross sections of state-to-state transitions in O_3^* collided with a quencher (such as Ar atom). Here we present such cross sections for transitions between some of the upper states in ozone. This includes states of the symmetric stretch and the asymmetric stretch normal mode progressions, but also states of the local vibration mode progression observed closer to the dissociation threshold. We discuss properties of these cross sections in detail. We also show how to compute the stabilization rate coefficients k_{stab} and what is needed in order to approach the overall recombination rate constant κ . Finally, we compute κ but, due to primarily methodological character of the paper, we do not make a big deal of the value obtained. We focus on theoretical and computational methodology that permits to make these calculations affordable. Note that our calculations are done for a broad distribution of rotational excitations in O_3^* (up to $J = 90$) and the value of κ is converged with respect to included values of J . Recall that all previous quantum calculations were done for the non-rotating O_3^* only ($J = 0$).

We also hope that the dimensionally reduced model will be useful in the future studies of the isotope effect. The anomalously large isotope effect in the ozone forming reaction²⁵ is expected to be related to difference of zero-point energies in two reaction channels (e.g., left vs. right in $^{18}O + ^{16}O^{16}O \rightarrow ^{18}O^{16}O^{16}O \leftarrow ^{18}O^{16}O + ^{16}O$) and also to symmetry of O_3^* (e.g., $^{16}O^{18}O^{16}O$ vs. $^{18}O^{16}O^{16}O$). It appears that

in order to capture these effects we need only two explicitly treated vibrational degrees of freedom.²⁴ The bending motion is likely to be less relevant to the isotope effect and can be treated adiabatically. In this primarily methodological paper we study only one isotopomer of ozone – the symmetric molecule $^{16}\text{O}^{18}\text{O}^{16}\text{O}$. In the future we plan to carry out similar calculations for stabilization of the asymmetric isotopomer, $^{18}\text{O}^{16}\text{O}^{16}\text{O}$, in order to study the effect of molecular symmetry onto the recombination rate.

Another focus of this paper is on efficient calculation of the third-order thermal rate constant κ of the overall recombination reaction (6). Note that within the full quantum framework (6D wave packet or coupled-channel) this quantity would be extremely difficult to compute. Indeed, a number of independent quantum scattering calculations at different values of the $\text{O}_3^* + \text{Ar}$ collision energy would be needed, and each such calculation would have to include all rotational states of O_3^* (since the angular momentum quantum number J of O_3^* changes significantly during the stabilizing $\text{O}_3^* + \text{Ar}$ collisions). In our mixed quantum-classical method these computational difficulties are avoided by treating some degrees of freedom classically and following an efficient multi-dimensional sampling procedure (described in detail in this paper). The major quantum effects in O_3^* are still incorporated into the treatment.

The paper is organized as follows. We start by presenting in Sec. II the model for kinetics, with the purpose of showing what quantities have to be determined from the dynamics calculations. In Sec. III we describe the method of computing the recombination rate constant using our mixed quantum-classical method for collision dynamics. In Sec. IV we present results of calculations and discuss our findings. Major conclusions of the paper are summarized in Sec. V.

II. KINETICS

The recombination kinetics is described within the micro-canonical framework, where different metastable states of O_3^* (different scattering resonances) are treated as different chemical species. For each such state, the processes of formation from $\text{O} + \text{O}_2$, decay back to $\text{O} + \text{O}_2$, and quenching into the stable O_3 states are considered, and the corresponding rate constants are introduced (individually for each resonance O_3^*). Similar treatments of kinetics can be found in the papers by T Pack,^{40–42} Clary,^{33,34} and Babikov.^{16,20,22}

Figure 1 gives example of vibrational spectrum of $^{16}\text{O}^{18}\text{O}^{16}\text{O}$ computed using the reduced-dimensional model of ozone within our mixed quantum-classical framework for the rotational state characterized by $J = 30$, $K_a = 5$, and $K_b = 20$. In this case, four metastable states, trapped behind the centrifugal barrier, are seen in the region above the covalent well. These are states from 48 to 51. State 47 and all states below are bound in the covalent well (only three upper bound states are seen in Fig. 1). Two vdW states outside of the centrifugal barrier^{16,43–45} are also seen in Fig. 1. In principle, we can compute cross sections for all possible state-to-state transitions, namely: metastable-to-bound, metastable-to-metastable, metastable-to-vdW, and metastable-to-continuum (see Sec. III) and, similarly, all kinds of transitions originating

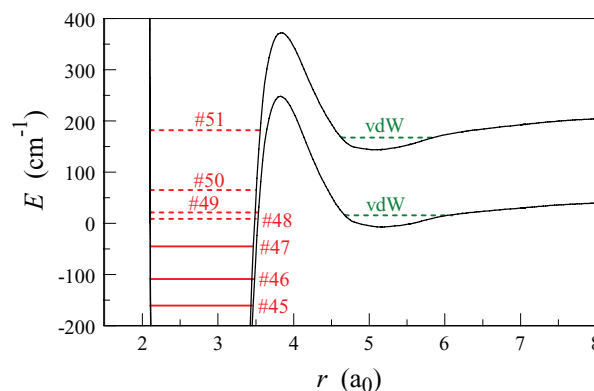


FIG. 1. Spectrum of states of $^{16}\text{O}^{18}\text{O}^{16}\text{O}$ with $J = 30$ ($K_a = 5$, $K_b = 20$) near threshold for dissociation. Slices of PES along two channels show the main covalent well and two shallow vdW wells. Bound states are shown by solid lines, while scattering resonances at energies above the threshold are shown by dashed lines. Energies of states and their vibrational character are given in Table II. In this model the overall rotation and the bending motion of ozone are treated adiabatically.

from the bound states and from the vdW states. An important question is: *Which transitions are really important for the recombination kinetics?*

We consider the low-pressure limit of the ozone forming reaction.^{17,46,47} From the experiment it is well known that the third-order rate constant κ for the overall reaction (6) shows no dependence on pressure of the bath gas $[\text{M}]$, consistent with the low-pressure model.^{17,46,47} In the low-pressure regime, fast pre-equilibrium is achieved between the $\text{O} + \text{O}_2$ reactants and each scattering resonance $\text{O}_3^*(i)$ at energy E_i . This process can be adequately characterized by introducing the micro-canonical equilibrium constant $K_{\text{eq}}(E_i)$ for each scattering resonance populated by the reaction (4). So, our first conclusion is that in the low-pressure regime there is no need to introduce, separately, the rate constants for formation and for decay of a scattering resonance (which would require computing the resonance lifetimes). Note that although this assumption should be applicable to ozone, it may not be valid for other molecules. Examples are known^{48–50} where a broad distribution of resonance lifetimes has effect on the reaction rates. In such cases the knowledge of the resonance lifetimes is required.

Second, due to the same low-pressure assumption, all the state-to-state transitions in O_3^* due to $\text{O}_3^* + \text{M}$ collisions can be considered as minor processes and most of them can be neglected, except those few that lead to the final products. Such transitions describe the rate-determining step – stabilization of $\text{O}_3^*(i)$ into stable O_3 states and are characterized by second-order rate constants $k_{\text{stab}}^{(i)}$ in reaction (5). Third, the processes of re-excitation of O_3 back to O_3^* can also be ignored, because concentration of the product $[\text{O}_3]$ is assumed to be small compared to concentration of the reaction intermediate $[\text{O}_3^*]$, which is in fast equilibrium with reactants $[\text{O}] \cdot [\text{O}_2]$. Thus, in the low pressure regime, the third-order rate constant for the overall recombination reaction (6) can approximately be computed as^{16,34}

$$\kappa \approx \sum_i k_{\text{stab}}^{(i)} K_{\text{eq}}(E_i), \quad (7)$$

where the sum is over all scattering resonances, labeled here by index i .

The equilibrium constant for each resonance can be calculated statistically as ratio of partition functions for products and reactants:

$$K_{\text{eq}}(E_i) = \frac{Q_{\text{bend}}(2J+1)e^{-E_i/kT}}{Q_{\text{el}} Q_{\text{tr}} Q_{\text{rot}}}. \quad (8)$$

Denominator in Eq. (8) contains standard partition functions for electronic, translational, and rotational states of $\text{O} + \text{O}_2$. Numerator in Eq. (8) includes the vibrational bending partition function introduced in order to compensate for the adiabatic treatment of bending in our reduced-dimensional approach. Remaining part of the numerator in Eq. (8) accounts for thermal population of each ro-vibrational state $\text{O}_3^*(i)$ at energy E_i . The factor of $2J+1$ in Eq. (8) accounts for space degeneracy of each rotational state.

The values of $k_{\text{stab}}^{(i)}$ needed for Eq. (7) are easily computed if the stabilization cross sections $\sigma_{\text{stab}}^{(i)}$ for each resonance $\text{O}_3^*(i)$ are known

$$k_{\text{stab}}^{(i)} = \frac{\nu(T, \sigma_{\text{stab}}^{(i)})}{[M]} = \sigma_{\text{stab}}^{(i)} \left(\frac{8kT}{\pi \mu} \right)^{1/2}. \quad (9)$$

Here $\nu(T, \sigma_{\text{stab}}^{(i)})$ is the temperature dependent stabilizing collision frequency, μ is the reduced mass of the $\text{Ar} + \text{O}_3^*$ collision. Using Eqs. (8) and (9), we can rewrite Eq. (7) in the following form:

$$\kappa = C \sum_i \sigma_{\text{stab}}^{(i)} (2J+1) e^{-E_i/kT}, \quad (10)$$

where the constant

$$C = \left(\frac{8kT}{\pi \mu} \right)^{1/2} \frac{Q_{\text{bend}}}{Q_{\text{el}} Q_{\text{tr}} Q_{\text{rot}}} \quad (11)$$

measured in the units of cm^4/s , was introduced for convenience.

The sum in Eq. (10) is over all metastable rotational-vibrational states, but in our mixed quantum-classical method the rotational and vibrational degrees of freedom are treated differently. The vibrational states are quantized, while the rotational states are treated quasi-classically and their spectrum is, strictly speaking, continuous. Furthermore, in our reduced-dimensional model of ozone there are only a handful of vibrational states, while there are few hundred of rotational states for each vibrational state. Due to these two reasons it is useful to split the sum of Eq. (10) in the following way:

$$\kappa = \sum_n \kappa^{(n)}, \quad (12)$$

where

$$\kappa^{(n)} = C \sum_i (2J+1) e^{-E_i/kT} \sigma_{n,\text{stab}}^{(i)}. \quad (13)$$

Index n labels vibrational states and $\kappa^{(n)}$ represents contribution of each vibrational state into the recombination process. From now on, index i labels only rotational states of a given vibrational state but, as before, just the metastable states at energies above the threshold (scattering resonances) are included into the sum of Eq. (13).

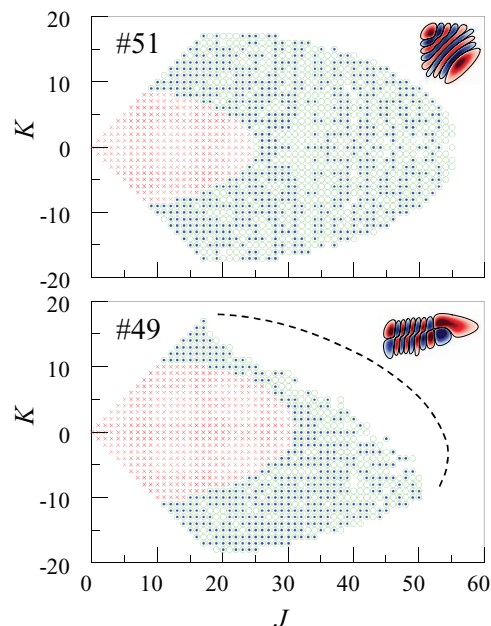


FIG. 2. Schematic of (J, K) -distribution for two upper vibrational states. Red \times indicate values of J and K that correspond to bound states (energy is below threshold). Blue dots and green circles are used to show the values of J and K that correspond to scattering resonances (energy is above threshold). See text for details. State 51 is a normal mode state, while state 49 is a local mode state. Insets show their vibrational wave functions in the bond length coordinates.

For example, consider a non-rotating ozone molecule and focus on a given bound vibrational state $\text{O}_3(n)$ slightly below threshold for dissociation onto $\text{O} + \text{O}_2$. Since this state is below the threshold it cannot be populated from $\text{O} + \text{O}_2$ reactants, and cannot contribute to the recombination. However, as rotational excitation of ozone increases, energy of this state rises (due to rotational potential) and at some point this state may become a resonance $\text{O}_3^*(n, i)$ above the dissociation threshold, where it will receive population from $\text{O} + \text{O}_2$ and will start contributing to the recombination process. This phenomenon is illustrated by extensive calculations presented in Fig. 2 (detailed discussion of this figure is postponed till Sec. III). In the non-rotating O_3 ($J=0$) the vibrational state 51 is the upper bound state. Our calculations showed that this vibrational state remains bound for $J \leq 8$, no matter what the value of K is (see Fig. 2). For $J=9$ this state may become metastable but only if $K=J$, which corresponds to rotation of molecule around the principal axis with small value of the moment of inertia (see Fig. 3(a)). For the values of J in the range $9 \leq J \leq 24$ the state 51 is metastable only if K is sufficiently large (see Fig. 2). For $J \geq 25$ this state is always metastable, even if $K=0$, which correspond to rotation of molecule around the principal axis with large value of the moment of inertia (see Fig. 3(b)). Thus, the vibrational state 51 should be included into the sum of Eq. (12) only in conjunction with certain rotational states, which defines what we will call below the (J, K) -distribution of resonances. Figure 2 gives examples of (J, K) -distribution for two vibrational states: 51 and 49.

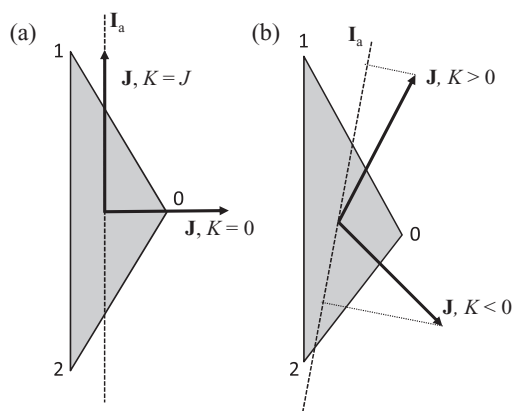


FIG. 3. Examples of relative orientations of the triatomic molecule (gray triangle), the angular momentum vector \mathbf{J} , and its projection K onto the principal axis of inertia \mathbf{I}_a for: (a) a symmetric normal mode state; (b) an asymmetric local mode state.

Note that the factor

$$w^{(i)} = (2J + 1) e^{-E_i/kT} \quad (14)$$

in front of cross section in Eq. (13) is unitless. It determines importance of each rotational state in the recombination process and, for convenience, can be introduced to further simplify the final formula:

$$\kappa^{(n)} = C \sum_i w^{(i)} \sigma_{n,stab}^{(i)}. \quad (15)$$

Note that in the (J, K) -distribution of Fig. 2 we showed only those metastable states that have $w^{(i)} > 2\%$ of w_{max} for this vibrational state, i.e., only those that are important. For example, for state 51 the maximum weight w_{max} is found for the rotational state characterized by $J = 25$ and $K = 0$ (which is the left-most state on the $K = 0$ axis in the upper frame of Fig. 2). For the state characterized by $J = 55$ and $K = 0$ (the rightmost state) the weight is about 50 times smaller. In general, states with medium values of J and small values of K have larger weights.

A practical way of employing Eq. (15) is presented in the next section. Here, for the sake of completeness, we give equations used to compute the partition functions of Eq. (11). Standard partition functions for electronic, translational and rotational states of $O + O_2$ were used,

$$Q_{el} = 3[5 + 3 \exp(-227.6/T) + \exp(-325.9/T)], \quad (16)$$

$$Q_{tr} = \left(\frac{\mu_{O+O_2} k_B T}{2\pi \hbar^2} \right)^{3/2}, \quad (17)$$

$$Q_{rot} = \frac{k_B T}{B \hbar^2}, \quad (18)$$

leading to $Q_{el} = 20.2$, $Q_{tr} = 3.50 \times 10^{25} \text{ cm}^{-3}$, and $Q_{rot} = 153.9$ at room temperature, $T = 300 \text{ K}$. In order to compute Q_{bend} the harmonic oscillator model was used,

$$E_{bend} = \left(v + \frac{1}{2} \right) \omega_{bend} \hbar, \quad (19)$$

with frequency of 707.2 cm^{-1} , which corresponds to the bending mode of O_3^* in the covalent well. This expression was employed to generate a pseudo-3D spectrum of O_3^* , based on the dimensionally reduced (2D) spectrum computed numeri-

cally. The partition function was determined based on the ratio between the density of states in the 3D and 2D spectra. At the vicinity of dissociation threshold the value of $Q_{bend} = 6.83$ was obtained. Using this information, the numerical value for the constant C was obtained according to Eq. (11): $C = 3.35 \times 10^{-24} \text{ cm}^4/\text{s}$.

The last thing we want to mention in this section is that the microcanonical treatment of recombination employed above (namely, Eq. (8) for the equilibrium constant) is based on statistical assumption – the ergodic hypothesis, which assumes that the population is equally distributed between all energetically accessible states. However, it has already been pointed out by several authors, based on computational and experimental results,^{51–54} that the ozone forming reaction exhibits several pronounced non-statistical features. Some O_3^* states, although accessible energetically, may not be accessible dynamically. In such a case, the microcanonical treatment needs some *educated extension* in order to comply with the expected behavior. In Sec. IV C we, first, apply the microcanonical treatment exactly as it is described above and demonstrate that it leads to a non-physical result. Next, in Sec. IV D, we propose a method for fixing the problem, by taking into account information about the dynamics of O_3^* formation, obtained from the complementary classical trajectory simulations.

III. COLLISION DYNAMICS

A straightforward way of using Eq. (15) would be to compute converged cross section $\sigma_{stab}^{(i)}$ for stabilization of each ro-vibrational scattering resonance $O_3^*(n, i)$, and then compute their weighted sum. We did compute such converged cross sections in the previous work¹⁶ for stabilization of the vdW states, and we have also done it for several resonances $O_3^*(n, i)$ on early stages of this work. But soon we realized that such approach is not optimal. Indeed, many of the metastable states in the sum of Eq. (15) have very small weights (e.g., states at larger values of J and K). Why to do calculations for all states at the same level of accuracy? A much better approach is to compute, at once, the entire sum of Eq. (15), worrying only about convergence of the sum as a whole, which directly reflects convergence of the rate constant $\kappa^{(n)}$ for a given vibrational state, summed over all rotational states. The weights $w^{(i)}$ can be used in order to emphasize the most important rotational states. It appears that this approach is very efficient and is relatively straightforward to implement within the framework of our mixed quantum-classical method, which is discussed next. (The mixed quantum-classical method itself will not be reviewed here; the readers are encouraged to read Refs. 12 and 16.)

A. Efficient multi-dimensional sampling

In the mixed quantum-classical method^{12,16} the probabilities of vibrational state-to-state transitions, for each collision trajectory, are obtained by projecting the final wave packet $\Psi_n(t_{fin})$ onto the vibrational eigenstates $\Phi_{n'}$ of the final rotational state:

$$p_{n,n'} = |\langle \Phi_{n'} | \Psi_n(t_{fin}) \rangle|^2. \quad (20)$$

Index n means that at the initial moment of time (before the $O_3^* + M$ collision) the wave packet was started in a given vibrational eigenstate:

$$\Psi_n(t_{\text{ini}}) = \Phi_n. \quad (21)$$

Probabilities $p_{n,n'}$, averaged over the collision trajectories, are used to compute the state-to-state transition cross sections:

$$\sigma_{n,n'} = \pi b_{\text{max}}^2 \frac{\sum_{\text{traj}} b p_{n,n'}}{\sum_{\text{traj}} b}. \quad (22)$$

Several other types of cross sections can be computed in a similar manner. For example, the cross section for transition from a given vibrational state of covalent well into the vdW well, labeled here as $\sigma_{n,\text{vdW}}$, is computed using equation similar to Eq. (22), but with cumulative probability for transitions into all states n' of the vdW well:

$$P_{n,\text{vdW}} = \sum_{n' \in \text{vdW}} p_{n,n'}. \quad (23)$$

The dissociation cross section $\sigma_{n,\text{diss}}$ is computed using dissociation probability for each trajectory,

$$P_{n,\text{diss}} = 1 - \sum_{n'} p_{n,n'}, \quad (24)$$

where the sum is over all bound states and narrow scattering resonances. Finally, we define the vibrational stabilization probability as

$$P_{n,\text{stab}} = \sum_{n' < n} p_{n,n'}. \quad (25)$$

This is used to calculate the stabilization cross section $\sigma_{n,\text{stab}}$ for every vibrational state n .

The sum over trajectories in Eq. (22) represents sampling over impact parameter, incident direction and energy of the projectile (the quencher M). Ozone molecule is a target, initially at rest at the origin of the laboratory reference frame. In a straightforward approach we used in the past^{12,16} all trajectories start with initial wave packet in the same chosen initial rotational-vibrational state $\Phi_n^{(i)}$. The state-to-state cross sections computed in this way are associated with given rotational state (i) and could be labeled as $\sigma_{n,n'}^{(i)}$.

For this work we devised a more complicated sampling procedure that allows computing directly the thermal rate constant $\kappa^{(n)}$ for each vibrational state, without computing converged cross sections $\sigma_{n,n'}^{(i)}$ for each initial rotational state. Our procedure involves simultaneous random sampling from the following four distributions:

- (i) The impact parameter of M is sampled uniformly in the range between $b = 0$ and $b_{\text{max}} = 15$ a.u.
- (ii) The incident direction of M is sampled isotropically as described in Ref. 16.
- (iii) The $O_3^* + M$ collision energy is sampled from thermal distribution at $T = 300$ K as explained in Appendix A of Ref. 16.
- (iv) The initial rotational state i of $O_3^*(n, i)$ is sampled quasi-classically from the (J, K) -distribution, like those shown in Fig. 2, taking into account the weighting factor $w^{(i)}$ of Eq. (14).

Note that, before starting this sampling procedure, one has to run quite extensive calculations of ro-vibrational states of O_3^* for all relevant values of J and K in order to generate the (J, K) -distributions (like those in Fig. 2) for all relevant vibrational states n . Energies and wave functions of ro-vibrational states have to be determined. If energy E_i is above the dissociation threshold the state is assigned as scattering resonance and is given a non-zero sampling weight according to Eq. (14). Its wave function $\Phi_n^{(i)}$ is used to set up the initial wave packet. Of course, in many aspects this procedure is similar to usual sampling for the classical trajectory simulations.⁵⁵ But the rotational weighting factors $w^{(i)}$ and the quantized vibrational states are the features specific to our mixed quantum-classical implementation.

This way of sampling allows obtaining directly the contribution of each vibrational state into the thermal rate constant of recombination as

$$\kappa^{(n)} = C\pi b_{\text{max}}^2 \sum_{\text{all } i} w^{(i)} \left(\frac{\sum_{\text{one } i} b P_{n,\text{stab}}}{\sum_{\text{one } i} b} \right). \quad (26)$$

This equation is obtained by combining Eqs. (15), (22), and (25). The outer sum in Eq. (26) is over all sampled rotational states, while the inner sums are accumulated separately for different rotational states, as the overall sampling procedure goes on.

Figure 4 gives example of convergence studies for $\kappa^{(n)}$ for two vibrational states of different character. State 51 is a normal-mode state with a relatively compact wave function, while the state 49 is a local-mode state with wave function extended more along one coordinate and less along the other (see insets in Fig. 2; better pictures of wave functions for these states can be found in Ref. 12, Fig. 3). Figure 4 shows that after sampling $N_{\text{traj}} = 30\,000$ trajectories the statistical errors of both $\kappa^{(49)}$ and $\kappa^{(51)}$ drop to below 2% of their absolute values (note the log scale). In fact, we see that even as few as $N_{\text{traj}} = 5000$ trajectories are sufficient in order to produce very reasonable results, with statistical errors within 5%. Comparison of $\delta\kappa^{(51)}$ vs. $\delta\kappa^{(49)}$ in Fig. 4 shows that convergence is more monotonic for the compact state 51, while the statistical error of the extended state 49 exhibits more pronounced fluctuations. This is understood, since the collision geometry is expected to matter more for the state described by a

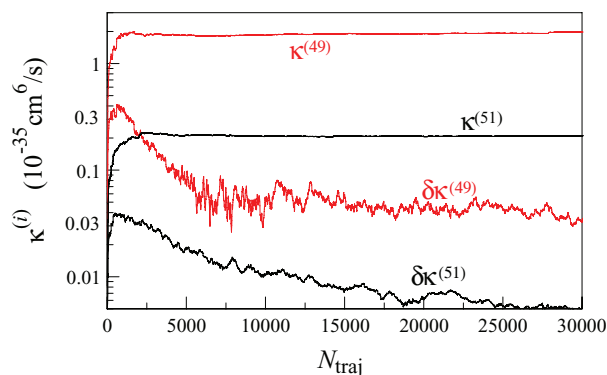


FIG. 4. Convergence studies for contributions $\kappa^{(n)}$ of two upper vibrational states into the third-order recombination rate constant. Corresponding statistical errors are shown as $\delta\kappa^{(n)}$.

“shaped” wave function, and is expected to matter less for the state described by a “shape-less” wave functions.

Efficiency of this sampling procedure is demonstrated by the following comparison. If we would decide to compute individually the converged cross section for each initial rotational state using Eq. (22), we would have to sample about 7000 trajectories for each initial rotational state. The number of rotational states to sample is about 340 for the vibrational state 51 and is about 420 for the vibrational state 49 (see Fig. 2). Thus, the computational advantage of our direct approach is dramatic: it allows decreasing the number of trajectories by a factor of around 80–100. Of course, the distribution of 30 000 trajectories of the sample over the initial rotational states is not uniform. In the example presented in Fig. 4, the number of trajectories per rotational state is at the level of few hundred for the most important states (small values of J and K), and is at the level of only few trajectories for the least important states (large values of J or K).

B. Properties of (J, K) -distributions

Note that sampling of the initial rotational states described above employs a symmetric top rotor assumption for O_3^* . Namely, it is assumed that $K_b = K_c$ and only the values of J and $K = K_a$ have to be sampled. This is done in order to simplify the sampling procedure and avoid sampling simultaneously three moieties: J , K_a , and K_b . This approximation is justified by the fact that real ozone is, indeed, very close to the symmetric top rotor⁵⁶ and that the components K_b and K_c of the angular momentum vector J change rapidly due to rotation of O_3^* (during the pre-collision dynamics), while the value of K_a remains approximately constant. Note, however, that the symmetric top assumption is used only for the *initial* semi-classical sampling. During the course of dynamics the ozone molecule rotates freely in our calculations as a “fluid” classical rotor without any constrains (see Ref. 12).

Also note that the (J, K) -distribution for the vibrational state 51 is symmetric with respect to sign of K . This is because state 51 is characterized by a symmetric wave function (see insets in Fig. 2 here, or Fig. 3 in Ref. 12). Due to this symmetry, the state with

$K < 0$ has the same energy and nature (bound or metastable) as the corresponding state with $K > 0$. In practice the sampling of rotational states for such symmetric vibrational states can be restricted to one half of the (J, K) -distribution (e.g., to $K \geq 0$ space).

In contrast, the (J, K) -distribution for state 49 (lower frame in Fig. 2) is non-symmetric with respect to the sign of K . This is because this state belongs to progression of the local-mode states. Such states come in pairs (exactly degenerate at $J = 0$ and non-degenerate when $J > 0$) and wave function of each state of the pair is non-symmetric. This feature leads to different energies associated with $K > 0$ and $K < 0$ rotations, as illustrated in Fig. 3(b). Rotation with $K > 0$ occurs around axis that crosses longer O–O bond (bond 0–1 in Fig. 3(b)), while the rotation with $K < 0$ occurs around axis that crosses shorter O–O bond (bond 0–2 in Fig. 3(b)). As result, energy of the $K > 0$ state is slightly lower, compared to the $K < 0$ state. Extensive calculations presented in Fig. 2 for state 49 show that quite often the $K < 0$ states are metastable, while the $K > 0$ states with same values of $|K|$ are bound. For example, the state 49 with $J = 20$ and $K = -9$ is already metastable, while the state 49 with $J = 20$ and $K = +9$ is still bound (see Fig. 2). This effect makes the border between bound and metastable states in Fig. 2 slightly asymmetric with respect to the sign of K for the local-mode state 49 (while the border is exactly symmetric for the normal mode state 51). Thus, in the sampling of initial rotational states we have to sample both $K > 0$ and $K < 0$ parts of the asymmetric (J, K) -distribution for the vibrational state 49. Now recall that the local-mode state 49 has a degenerate twin brother (state 50, see Table I below). The good news is that if both $K > 0$ and $K < 0$ parts of the asymmetric (J, K) -distribution for the vibrational state 49 have been sampled, the calculations for state 50 are not required, since the results must be equivalent: $\kappa^{(49)} = \kappa^{(50)}$.

Finally, an important feature of the (J, K) -distribution for state 49 is that some scattering resonances are missing in the range of large positive values of K . This region of the (J, K) -distribution is encircled by dashed line in the lower frame of Fig. 2. Detailed analysis has shown that such states

TABLE I. Rotationally averaged cross sections $\bar{\sigma}_{n,n'}$ (a_0^2) for vibrational state-to-state transitions.

Final state	Initial state									
	51	49, 50	48	46, 47	45	44	43	41, 42	39, 40	38
51	...	0.822	2.885	0.095	0.113	0.008	0.008	0.001	0.001	0.039
49, 50	0.145	...	2.547	12.571	1.595	0.163	0.140	0.047	0.051	0.001
48	2.299	2.827	...	2.818	6.513	0.358	0.303	0.015	0.013	0.048
46,47	0.072	19.440	4.325	...	18.215	1.099	0.909	0.231	0.179	0.004
45	0.072	1.861	6.593	13.215	...	6.817	5.019	0.030	0.029	0.008
44	0.003	0.134	0.311	2.191	7.855	...	67.314	0.167	0.178	0.008
43	0.003	0.114	0.200	1.693	3.743	70.727	...	0.285	0.292	0.014
41, 42	0.003	0.046	0.019	0.226	0.077	0.739	0.763	...	56.807	0.904
39, 40	0.002	0.043	0.016	0.133	0.059	0.757	0.739	56.085	...	2.646
38	0.095	0.002	0.021	0.004	0.004	0.015	0.016	0.724	2.635	...
37 and below	0.053	0.701	0.205	0.088	0.173	0.302	0.275	1.440	2.054	16.693
All vdW states	1.095	0.549	0.134	0.174	0.013	0.010	0.002	0.001	0.001	0.000
All continuum	44.078	125.374	53.515	123.534	59.935	61.287	43.365	80.163	85.990	50.415

become short lived due to the following effect: When the molecule is characterized by an asymmetric local-mode wave function, like that of state 49, the shape of rotational potential depends on the sign of K (again, due to effect illustrated in Fig. 3(b)). Negative values of K give very broad centrifugal barrier able to support long-lived scattering resonances. Positive values of K result in a relatively narrow barrier. In the vicinity of its top the vibrational states couple to continuum efficiently, become short lived and disappear from the (J, K) -distribution of narrow resonances.

C. Deeper insight into the stabilization process

Detailed insight into the process of stabilization can be obtained by computing, for each initial and final vibrational states n and n' , the state-to-state transition cross sections averaged over all rotational states:

$$\tilde{\sigma}_{n,n'} = \frac{\sum_i w^{(i)} \sigma_{n,n'}^{(i)}}{\sum_i w^{(i)}}. \quad (27)$$

These moieties are not used in calculations of rate constants (the rate constants are computed directly) but they are very useful to have in order to represent the recombination process in detail using the convenient units of cross section. In a similar way, rotationally averaged cross sections $\tilde{\sigma}_{n,\text{stab}}$, $\tilde{\sigma}_{n,\text{diss}}$, and $\tilde{\sigma}_{n,\text{vdW}}$ for stabilization, dissociation and for transition into the vdW well, respectively, can also be computed.

Even deeper insight can be obtained by exploring, as a functional dependence, the following moiety:

$$F_{n,\text{stab}}(J, K) = w^{(i)} \sigma_{n,\text{stab}}^{(i)}. \quad (28)$$

Note that although the individual values of $\sigma_{n,\text{stab}}^{(i)}$ for different rotational states i are not converged in our calculations, the product $w^{(i)} \sigma_{n,\text{stab}}^{(i)}$ is a well behaved function of J and K , suitable for analysis. It shows how the stabilization cross section changes, as a function of quantum numbers J and K .

Quite often the quenching process is characterized in terms of the energy transfer functions.⁵⁷⁻⁶² While we do not use the energy transfer functions in our calculations of the rate coefficient, we still compute and discuss them in this paper for deeper insight and for the purpose of comparison with experiment and/or with calculations by other workers in the future. For each initial vibrational state we compute the differential (over energy) *probability distribution function* for energy transfer as

$$\bar{P}_{n,\text{stab}}(\Delta E) = \frac{\sum_{n' < n} P_{n,n'}}{\delta E}. \quad (29)$$

Here $\Delta E = E_{n'} - E_n$ is the extent of the state-to-state rovibrational energy transfer, $p_{n,n'}$ is the corresponding probability. Analysis of single quantum-classical trajectory produces a discrete function $\bar{P}_{n,\text{stab}}(\Delta E)$ that looks like a set of ‘‘sticks’’ at energies of the final vibrational states labeled by n' . Calculations for multiple trajectories are binned into a common histogram over coordinate ΔE with the box size δE , in

order to produce a nearly continuous function $\bar{\sigma}_{n,\text{stab}}(\Delta E)$:

$$\bar{\sigma}_{n,\text{stab}}(\Delta E) = \frac{\pi b_{\text{max}}^2 \sum_{\text{all } i} w^{(i)} \left(\frac{\sum_{\text{one } i} b \bar{P}_{n,\text{stab}}}{\sum_{\text{one } i} b} \right)}{\sum_{\text{all } i} w^{(i)}}, \quad (30)$$

which represents the *differential (over energy) cross section* of energy transfer. Various initial rotational states of the (J, K) -distribution are taken into account by summing results of all trajectories in the sample. This analysis is conducted separately for different initial vibrational states n (i.e., different energy transfer functions are obtained for different scattering resonances). Note that $\bar{\sigma}_{n,\text{stab}}$ is not an average over the initial rotational states, but is a weighted sum that correlates with the third-order rate coefficient $\kappa^{(n)}$ in Eq. (26). In fact, the value of $\kappa^{(n)}$ can be recovered (indirectly) from $\bar{\sigma}_{n,\text{stab}}$ as

$$\kappa^{(n)} = C \int_{-\infty}^{+\infty} \bar{\sigma}_{n,\text{stab}}(\Delta E) d\Delta E, \quad (31)$$

where C is the constant introduced above.

Also note that the sum of Eq. (29) takes into account only the vibrationally inelastic transitions downhill, $n' < n$ (vibrational stabilization), in accordance with discussion of the recombination kinetics given above in Sec. II. If the overall energy transfer is of interest, the sum of Eq. (29) should also include the vibrationally elastic channel, $n' = n$, and the excitation channels, $n' > n$. The differential (over energy) cross sections that include all channels of energy transfer will be denoted as $\bar{\sigma}_{n,\text{tran}}$. In the vicinity of elastic peak it is usual to fit such $\bar{\sigma}_{n,\text{tran}}(\Delta E)$ dependence by an analytical double-exponential function:¹⁶

$$\bar{\sigma}_{n,\text{tran}}(\Delta E) = \bar{\sigma}_{n,\text{tran}}(0) \left(\exp \left\{ -\frac{|\Delta E|}{\gamma} \right\} + c \exp \left\{ -\frac{|\Delta E|}{d} \right\} \right). \quad (32)$$

The values of fitting coefficients $\bar{\sigma}_{n,\text{tran}}(0)$, γ , c , and d are reported.

Finally, we would like to stress that the *second-order rate coefficient* for energy transfer, $k_{n,\text{tran}}(\Delta E)$, frequently used in the literature,⁵⁷⁻⁶² can easily be obtained from our $\bar{\sigma}_{n,\text{tran}}(\Delta E)$ as

$$k_{n,\text{tran}}(\Delta E) = \left(\frac{8kT}{\pi \mu} \right)^{1/2} \bar{\sigma}_{n,\text{tran}}(\Delta E). \quad (33)$$

This expression follows from Eq. (9).

IV. RESULTS AND DISCUSSION

For the reason that will become clear in Sec. IV C below, we focus on collisional quenching of resonances that possess the vibrational character of ten upper vibrational states of ozone.¹⁶ At $J = 0$ all these states are bound but they become scattering resonances as rotational excitation lifts their energies above the dissociation threshold (see Fig. 2). Energies of these states for $J = 0$ are given in the second column of Table II. The upper vibrational state, state 51, is only 238.2 cm⁻¹ below the dissociation threshold. The lowest of these states, state 38 is at energy 1237.5 cm⁻¹ below the

TABLE II. Contributions of vibrational states into the third-order recombination rate constant.

State	E_{vib} (cm ⁻¹)	State character, quanta	N_{traj}	$\tilde{\sigma}_{n,\text{stab}}$ (a ₀ ²)		$\kappa^{(n)}$ (10 ⁻³⁵ cm ⁶ /s)		
				Computed	Interpolated	Statistical	Dynamical	Rotational
51	-238.2	N (8, 0)	31202	2.748	2.852	0.335	0.315	0.107
49, 50	-351.8	L (8, 1)	35701	25.168	24.983	2.813	2.336	0.519
48	-406.3	N (7, 1)	45238	11.691	11.808	1.664	1.274	0.237
46, 47	-452.8	L (10, 0)	41500	17.550	18.733	2.377	1.685	0.273
45	-570.6	N (6, 2)	38826	11.912	12.780	1.688	0.970	0.112
44	-731.0	N (5, 3)	24328	72.541	76.583	13.579	5.963	0.407
43	-781.7	N (4, 4)	36622	1.793	1.899	0.354	0.144	0.009
41, 42	-956.0	L (9, 0)	37674	58.249	63.152	12.024	3.703	0.120
39, 40	-1076.9	L (7, 1)	32866	4.689	8.696	1.435	0.344	0.006
38	-1237.5	N (7, 0)	25443	16.693	17.416	3.887	0.605	0.010
Total:						58.805	25.407	2.717

threshold. Six of these states belong to progression of the normal mode excitations with the number of quanta between 4 and 8 in the symmetric stretching mode and between 0 and 4 in the asymmetric stretching mode. The remaining four states belong to progression of the local mode vibrations that correlate with the asymptotic O + O₂ reactants. Each of such local-mode state is, in fact, a pair of states degenerate at $J = 0$, but they become non-degenerate as rotational excitation increases: 49–50, 46–47, 41–42, and 39–40. For these states, the number of quanta in the local O₂ mode is between 0 and 1, while the number of quanta in the O · · O₂ mode is between 7 and 10. In the reduced-dimensionality model the bending mode is treated adiabatically and is not excited. The local zero-point energy of bending is however, included, as explained in Ref. 12.

A. Rotationally averaged cross sections

Table I contains a 10 × 10 matrix of rotationally averaged cross sections $\tilde{\sigma}_{n,n'}$ computed for state-to-state transitions between the upper ten vibrational states. Calculations for each column of Table I were carried out separately, i.e., the (J, K)-sampling was done independently for each initial vibrational state. The final vibrational states in each column of Table I are accessed by spectral analysis of final wave packets, as it was explained above in Sec. III. Note that the elastic cross sections $\tilde{\sigma}_{n,n}$ suffer from the well-known problem of divergence due to the elastic scattering peak.⁶³ Their magnitudes depend on value of the maximum impact parameter b_{max} in Eq. (22) and, therefore, are quite meaningless. For this reason, the elastic cross sections were not included into Table I. We just want to mention here that for $b_{\text{max}} = 15a_0$ used in these calculations the values of elastic cross sections were in the range between 550 and 650 a_0^2 .

Several features of the state-to-state matrix $\tilde{\sigma}_{n,n'}$ in Table I are worth noting. First of all, this matrix exhibits near symmetry, originating in the principle of macroscopic reversibility.^{17,40–42} Namely, the magnitudes of $\tilde{\sigma}_{n,n'}$ correlate with magnitudes of $\tilde{\sigma}_{n',n}$. For example, if we look at the two largest cross sections in Table I we will see that

$\tilde{\sigma}_{44,43} = 70.7 a_0^2$ correlates with $\tilde{\sigma}_{43,44} = 67.3 a_0^2$. Analogously, the magnitude of $\tilde{\sigma}_{41-42,39-40} = 56.1 a_0^2$ correlates with magnitude of $\tilde{\sigma}_{39-40,41-42} = 56.8 a_0^2$, while the magnitude of $\tilde{\sigma}_{49-50,46-47} = 19.4 a_0^2$ correlates with magnitude of $\tilde{\sigma}_{46-47,49-50} = 12.6 a_0^2$. Finally, the value of $\tilde{\sigma}_{46-47,45} = 13.2 a_0^2$ correlates with $\tilde{\sigma}_{45,46-47} = 18.2 a_0^2$. These four pairs of cross sections, all with magnitudes above 10 a_0^2 , are most important in Table I. Furthermore, in Table I there are ten other pairs of cross sections with magnitudes in the range between 1 a_0^2 and 8 a_0^2 . In all those cases we also see correlation between $\tilde{\sigma}_{n,n'}$ and $\tilde{\sigma}_{n',n}$.

Second property is that the $\tilde{\sigma}_{n,n'}$ matrix is close to diagonal. The dominant cross sections usually correspond to transitions into the nearest state, $\tilde{\sigma}_{n,n\pm 1}$. In several cases the largest cross section is observed for transition into next to the nearest state, $\tilde{\sigma}_{n,n\pm 2}$, which represents the third major feature of the matrix. Examples of these special cases are: $\tilde{\sigma}_{49-50,46-47} > \tilde{\sigma}_{49-50,48}$ and $\tilde{\sigma}_{48,45} > \tilde{\sigma}_{48,46-47}$. We found that in such cases the initial state of a given character is surrounded by states of another character. For example, the *local-mode* state 49–50 is always surrounded by the *normal-mode* states above and below: states 51 and 48. The closest local-mode state is 46–47, which corresponds to $\tilde{\sigma}_{n,n\pm 2}$. Similarly, the *normal-mode* state 48 is surrounded by the *local-mode* states above and below: states 49–50 and 46–47. The closest normal mode state is 45, which would also correspond to $\tilde{\sigma}_{n,n\pm 2}$. Several more examples can be found in Table I. In such cases we usually see that $\tilde{\sigma}_{n,n\pm 2} > \tilde{\sigma}_{n,n\pm 1}$. This property of the state-to-state matrix can be described as bias to preservation of the vibrational mode character during the quenching process.

Large value of cross section for transition between states 44 and 43 is explained by the energetic proximity of these states: they are only 50 cm⁻¹ apart, while the energy spacings between all other normal mode states are larger than 160 cm⁻¹. In this sense, the large values of $\tilde{\sigma}_{44,43}$ and $\tilde{\sigma}_{43,44}$ are rather accidental and cannot be explained by the vibrational character of states involved. In all other cases we found that cross sections for stabilization of the local mode states are larger than those for the normal mode states. This is explained by larger spatial extend of the local-mode wave functions. In

general, they will have larger cross sections for inelastic interaction with quencher.

Three lower rows of Table I give cross sections that can be written as $\tilde{\sigma}_{n,n' < 38}$, $\tilde{\sigma}_{n,\text{vdW}}$, and $\tilde{\sigma}_{n,\text{diss}}$. The first of these is the cumulative cross section for transitions into *all* vibrational states below the state 38. The value of this cross section is usually small for the upper states, but it increases as the initial state approaches state 38. Cross sections for transitions from the covalent well into the vdW well are all relatively small, with the largest being $\tilde{\sigma}_{51,\text{vdW}} = 1.10 a_0^2$, found for the upper vibrational state. Magnitudes of these cross sections drop monotonically to zero, as initial vibrational excitation drops to state 38. Cross sections for dissociation $\tilde{\sigma}_{n,\text{diss}}$, given in the last row of Table I, are all relatively large. Larger cross sections correspond to initial states of the local mode progression; their values range between $80 a_0^2$ and $125 a_0^2$. For initial states of the normal mode progression the dissociation cross sections are on order of $50 \pm 10 a_0^2$. Thus, the dissociation cross sections are larger for the local mode states than for the normal mode states, roughly by a factor of two. This is understood, since the local mode states correlate better with the products of dissociation: O + O₂.

In order to avoid confusion, we would like to repeat here, once again, that in all these calculations the initial states are ro-vibrational scattering resonances at energies above the dissociation threshold. For example, cross section $\tilde{\sigma}_{38,\text{diss}} = 50.4 a_0^2$ in Table I is not the cross section for dissociation of the vibrational state 38 at energy -1237.5 cm^{-1} below the threshold (such cross section would be very small). The $\tilde{\sigma}_{38,\text{diss}}$ is a rotationally averaged cross section for dissociation of ro-vibrational scattering resonances that possess the vibrational character of state 38 but are rotationally excited above the dissociation threshold. Such dissociation processes are highly probable, which is reflected by significant values of the corresponding cross sections. Similarly, cross section $\tilde{\sigma}_{38,\text{vdW}}$ represents transitions to vdW well originating from the ro-vibrational scattering resonances that possess the vibrational character of state 38. Our calculations (see Table I) showed that this cross section is equal to zero because, at the level of rotational excitation needed to raise the vibrational state 38 above the dissociation threshold, the shallow vdW well is so flattened by the centrifugal potential that it cannot support any states (no final vdW states are available).

B. Rotationally resolved cross sections

The values of stabilization cross sections $\sigma_{n,\text{stab}}^{(i)}$ for different initial rotational states i have also been obtained. Figure 5 shows the $F_{n,\text{stab}}(J, K)$ dependencies computed using Eq. (28) for the initial vibrational states 49 and 51. The most important contribution into the quenching process comes from those rotational states that lie close to the bound states on the (J, K) -distribution. They are characterized by intermediate and small values of K , and intermediate values of J . For example, for state 51 most important is the range of $22 < J < 32$ and $K < 10$, and the picture of $F_{n,\text{stab}}(J, K)$ is symmetric. For state 49 the picture of $F_{n,\text{stab}}(J, K)$ is asymmetric and shows more structure, with most important initial states in the range of $22 < J < 36$ and $K < 16$. Two examples presented

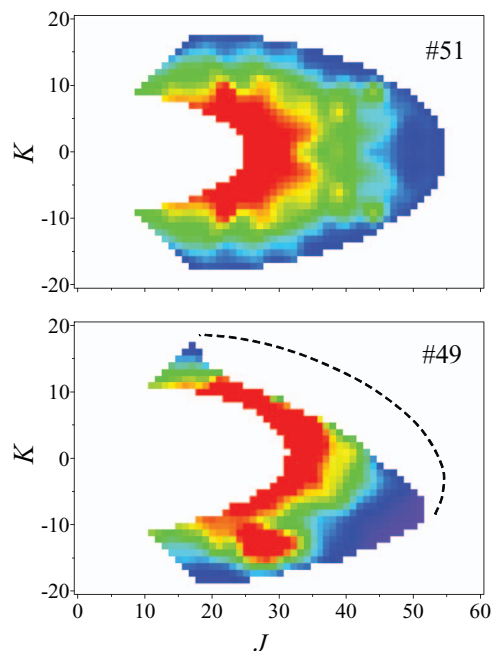


FIG. 5. Dependence of the rotationally weighted stabilization cross sections $w^{(i)}\sigma_{n,\text{stab}}^{(i)}$ on the quasi-classical quantum numbers J and K , as defined by Eq. (28). Results for two upper vibrational states are shown. Color indicates magnitude of the cross section, decreasing from red to violet.

in Fig. 5 are typical. The $F_{n,\text{stab}}(J, K)$ dependencies for other vibrational states look similar. The range of most important J -values shifts towards larger J as vibrational excitation drops.

At this point we would like to mention the problem we encountered computing the rotationally resolved cross sections $\sigma_{n,\text{stab}}^{(i)}$. In principle, the calculations have to be carried out for all possible rotational states i of the (J, K) -distribution for a given vibrational state n . However, the mixed quantum-classical calculations are set up in the opposite order.^{12,16} First, the quasi-classical rotational state is specified by choosing the values of J and K . Then, the quantum eigenvalue problem is solved to determine vibrational states. Finally, analysis of their wave functions allows identifying the vibrational state n needed to set up the initial wave packet for the mixed quantum-classical calculations of quenching.^{12,16} However, the massive calculations of (J, K) -distributions carried out in this work showed that, for some values of J and K , the needed vibrational state n was simply missing from the spectrum. Figure 2 illustrates this problem. Blue dots indicate those values of J and K where the state needed (either 49 or 51 in Fig. 2) was readily identified in the spectrum. It is seen very clearly that for many values of J and K the needed vibrational state was missing. Further analysis has shown that origin of this problem is technical. It does not represent any physical property of the spectrum of states, but reflects properties of the grid used to represent vibrational wave functions. In fact, it is known that a single grid cannot be used to represent equally well many scattering resonances. For example, the stabilization method of Clary employs multiple grids of changing length³³ in order to determine energies of narrow scattering resonances. We tried to vary the grid length and the density of points and, actually, were able to recover most

of the missing states. The states determined in this way are shown by green circles in Fig. 2. However, we found impractical to use different grids for different initial states in the calculations of the $O_3^* + M$ quenching. We have chosen to do the quenching calculations only for those rotational states i of the (J, K) -distribution where the needed vibrational states n were identified using single grid. In order to get results for those points of the (J, K) -distribution where the needed vibrational states were missing, we did interpolate the values of $\sigma_{n,\text{stab}}^{(i)}$ over the two-dimensional (J, K) -space.

Thus, the $F_{n,\text{stab}}(J, K)$ dependencies presented in Fig. 5 were obtained by interpolation, as described in the previous paragraph. In order to gauge the overall effect of interpolation we included two columns in Table II representing the rotationally averaged cross sections for stabilization $\tilde{\sigma}_{n,\text{stab}}$ computed before interpolation (using only blue points of (J, K) -distribution in Fig. 2) and after interpolation (using all points of the (J, K) -distribution). We see that for majority of the initial vibrational states the effect of interpolation is minor, within few percent. The only exception is state 39-40, where interpolation allows recovering a significant portion of magnitude of the $\tilde{\sigma}_{39-40,\text{stab}}$.

C. Thermal rate constant

Experimental value of the third order rate constant for recombination reaction forming isotopologue $^{16}O^{18}O^{16}O$ of ozone is $\kappa^{\text{exp}} = 65.3 \times 10^{-35} \text{ cm}^6/\text{s}$.^{64,65} There is an opinion,⁴⁶ supported by analysis of experimental data, that two different mechanisms contribute to this value. At room temperature the contribution of energy-transfer mechanism is expected to be about $\kappa^{\text{ET}} = 24.8 \times 10^{-35} \text{ cm}^6/\text{s}$. We use this value as a reference and compare our theoretical results against κ^{ET} .

The values of $\kappa^{(n)}$ computed for ten upper vibrational states are listed in Table II. The number of trajectories sampled in each case is also given. It ranges between 24 000 and 45 000. The actual number of trajectories needed for each initial vibrational state was determined by convergence studies, similar to those illustrated by Fig. 4. Our convergence criterion required adding trajectories until the statistical error of each computed $\kappa^{(n)}$ drops below 2% of its absolute value.

To some extent the magnitudes of $\kappa^{(n)}$ reflect the magnitudes of $\tilde{\sigma}_{n,\text{stab}}$. There is, however, an important difference between $\kappa^{(n)}$ and $\tilde{\sigma}_{n,\text{stab}}$. Cross section $\tilde{\sigma}_{n,\text{stab}}$ represents a weighted *average* over the rotational states, as defined by Eq. (27). In contrast, rate coefficient $\kappa^{(n)}$ represents a weighted *sum* over rotational states, as defined by Eq. (15). Among the values of $\kappa^{(n)}$ in Table II the largest is $\kappa^{(44)}$. This is consistent with large value of $\tilde{\sigma}_{44,\text{stab}}$, which is mostly due to $\tilde{\sigma}_{44,43}$ discussed above in detail. Among the other most important are contributions of the local mode states $\kappa^{(49-50)}$ and $\kappa^{(41-42)}$, consistent with large values of the corresponding cross sections $\tilde{\sigma}_{49-50,46-47}$ and $\tilde{\sigma}_{41-42,39-40}$ discussed above in detail.

According to Eq. (12), the direct sum of all $\kappa^{(n)}$ gives the value of third order rate constant for recombination. The sum of $\kappa^{(n)}$ over ten upper states (actually, fourteen states, due to four local-mode pairs) is given at the bottom of Table II. Note

TABLE III. Fitting parameters in a simple model for energy dependence of cross section for rotationally averaged vibrational state-to-state transitions.

Mode character	$A (a_0^2)$	$B (\text{cm}^{-1})$
L	77.2	99.3
N	146.0	52.5

that this number, $\kappa = 58.8 \times 10^{-35} \text{ cm}^6/\text{s}$, overshoots the experimental value of κ^{ET} by more than a factor of two already. But, according to Eq. (12), in addition to contribution of the ten upper states we also have to include contributions of the remaining thirty-seven lower states! We did not attempt to do the quenching calculations for states from 1 to 37 but we carried out extrapolation onto the lower states, using information from Tables I and II for ten upper states, in order to get a semi-quantitative insight onto the overall process. Namely, we assumed that for each initial state the quenching process is dominated by single transition into the vibrational state immediately below the initial state:

$$\tilde{\sigma}_{n,\text{stab}} \approx \tilde{\sigma}_{n,n-1}. \quad (34)$$

Then, using the data obtained for upper ten states, we analyzed the dependence of $\tilde{\sigma}_{n,n'}$ on $\Delta E = E_{n'} - E_n$ for states of the normal-mode progression and, separately, for the local-mode states. We found that those dependencies can be approximated by simple exponential model,

$$\tilde{\sigma}_{n,n'} = A \cdot \exp\{-(E_n - E_{n'})/B\}. \quad (35)$$

The values of fitting parameters A and B are given in Table III. Using this approach, the contribution of thirty seven lower states is estimated to be at least $356 \times 10^{-35} \text{ cm}^6/\text{s}$, leading to the total value of $\kappa = 415 \times 10^{-35} \text{ cm}^6/\text{s}$, which is a factor of seventeen larger than the experimental result κ^{ET} . Clearly, something is wrong in the straightforward approach of Eq. (12).

The origin of this problem is easy to spot, if one thinks carefully about the nature of O_3^* states formed in the thermal $O + O_2$ collisions. The main assumption of statistical approach is ergodic hypothesis, which assumes that all internal states of O_3^* , accessible at given collision energy of $O + O_2$, are equally populated and should be included into Eq. (7), and finally into Eq. (12). Although the internal degrees of freedom include rotation and vibration, the only thing that matters (in the straightforward statistical approach) is the total energy E_i used in the equilibrium constant of Eq. (8) and, finally, in the weighting function of Eq. (14). Consider example of $O + O_2$ colliding at total energy $E_i = k_B T$. This energy can be deposited into rotation and vibration of O_3^* , and statistical assumption is that a state with $E_{\text{rot}} = 3 k_B T/2$ and $E_{\text{vib}} = -k_B T/2$ will have the same population as, for example, a state with $E_{\text{rot}} = 31 k_B T$ and $E_{\text{vib}} = -30 k_B T$. (Recall that the covalent well of ozone is $\sim 10\,000 \text{ cm}^{-1}$ deep and such states are possible.) In fact, due to much larger rotational degeneracy factor $2J + 1$ in Eq. (8), the highly excited rotational states should (statistically) be even more important. This result, however, contradicts our knowledge of reaction dynamics. It is hard to imagine that the amount of vibrational energy this large can be deposited into rotation and, can survive there, without

being transferred into translational motion of bath gas and/or rotation of other molecules. It is well known that rotational energy is transferred readily from molecules to the bath gas, while the transfer of vibrational energy is much slower.

We strongly feel that the sum of Eq. (12) should be limited to *dynamically accessible* ro-vibrational states of O_3^* only, but there is no simple method for identifying such states. This question is further explored in Sec. IV D below. Here we want to show the result of trying a simple (statistical) fix to the problem.

One can try to assume that equilibrium is achieved between $O + O_2$ reactants and the *rotational* states of O_3^* only, without any vibrational energy transfer at all. In such case same equations apply, but the energy E_i in Eq. (8) for the equilibrium constant should represent the *rotational* energy of O_3^* states. In turn, the weight of each rotational state in Eq. (13) or Eq. (15), given by Eq. (14), should also be changed. In order to check the result of this assumption we generated new set of $\kappa^{(n)}$ by analytically re-weighting the contribution of each rotational state. Namely, the contribution of each rotational state in Eq. (26) was divided by the weight used in the sampling, $(2J + 1)\exp\{-(E_{\text{rot}} + E_{\text{vib}})/kT\}$, and then multiplied by new rotational weight $(2J + 1)\exp\{-E_{\text{rot}}/kT\}$. Values of such *rotational* $\kappa^{(n)}$ are given in the last column of Table II. They decrease quickly as we go down the vibrational spectrum, due to rotational Boltzmann distribution factor. We also see that now a very limited number of vibrational states contribute to the process – the ten states reported in Table II are well sufficient. The total value of this “rotational” rate constant, $\kappa = 2.72 \times 10^{-35} \text{ cm}^6/\text{s}$, is an order of magnitude smaller than the experimental value of κ^{ET} . However, this result sets up the lower limit and demonstrates that the vibrational energy transfer, although less efficient than the rotational energy transfer, is essential and must be included in order to reproduce experimental value of the recombination rate constant.

D. Failure of the ergodic hypothesis

In order to test the ergodic hypothesis we analyzed results of classical trajectory simulations for formation of O_3^* out of $O + O_2$ collided at room temperature. The main focus was on distribution of energy between rotational and vibrational degrees of freedom in the formed O_3^* . Figure 6 demonstrates our results. Vertical axis in Fig. 6 gives the internal vibrational energy of O_3^* relative to dissociation threshold (consistent with vibrational state energies given in Table II). Horizontal axis in Fig. 6 gives the rotational energy of O_3^* , relative to energy of non-rotating molecule. The color of points in the $(E_{\text{rot}}, E_{\text{vib}})$ -space demonstrates probability, with red showing the maximum probability and violet showing low probability. White area of the $(E_{\text{rot}}, E_{\text{vib}})$ -space shows the no trajectories zone (zero probability). We see that probability of forming rotationally excited O_3^* drops quickly as its rotational energy increases and vibrational energy decreases. We found very few events of O_3^* forming with rotational energy larger than $2k_B T$. We also found that almost never the vibrational energy of O_3^* drops further down than -1000 cm^{-1} . This means that only a few upper vibrational states of O_3^* can contribute

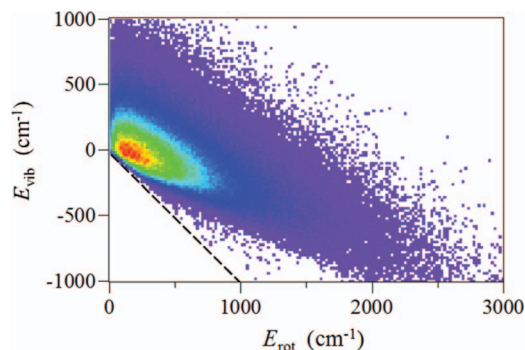


FIG. 6. Ro-vibrational energy distribution of the metastable O_3^* states, as dictated by classical dynamics simulations of $O + O_2$ collisions at room temperature. Dashed line indicates the dissociation threshold, where $E_{\text{tot}} = E_{\text{rot}} + E_{\text{vib}} = 0$.

to the recombination process. The maximum of $(E_{\text{rot}}, E_{\text{vib}})$ -distribution corresponds to $E_{\text{rot}} = 200 \text{ cm}^{-1}$, which is $\approx k_B T$, and $E_{\text{vib}} = -50 \text{ cm}^{-1}$, which is well above the state 51.

We see that the dynamical distribution of Fig. 6 is strongly non-ergodic. The ergodic distribution of Eq. (14), characterized by the total energy $E_{\text{tot}} = E_{\text{rot}} + E_{\text{vib}}$, would be close to isotropic along the diagonal line of the $(E_{\text{rot}}, E_{\text{vib}})$ -plot. As rotational excitation increases (going down the diagonal line in Fig. 6), the weight of ergodic distribution should increase, due to rotational degeneracy factor $2J + 1$. The dynamical distribution of Fig. 6 shows an opposite trend.

Clearly, this dynamical information should be included into calculations of the rate constants $\kappa^{(n)}$. In principle, one could try to build a dynamical weighting function $w_{\text{dyn}}(J, E_{\text{rot}}, E_{\text{vib}})$ based on results of the classical trajectory calculations and use it for re-weighting contributions of different ro-vibrational states based, simultaneously, on the values of their angular momentum J , rotational energy E_{rot} , and vibrational energy E_{vib} . As before, the contribution of each state in Eq. (26) could be divided by the old statistical weight $(2J + 1)\exp\{-E_{\text{tot}}/kT\}$ used in the sampling procedure and multiplied by new dynamical weight $w_{\text{dyn}}(J, E_{\text{rot}}, E_{\text{vib}})$. We found, however, that this approach is difficult to realize in practice because, due to low statistics, it is difficult to build a smooth three-dimensional distribution $w_{\text{dyn}}(J, E_{\text{rot}}, E_{\text{vib}})$. For practical reasons the reweighting procedure was implemented as explained next.

We constructed a one-dimensional *reweighting* function $w_{\text{dyn}}(E_{\text{vib}})$ using the multi-step procedure. First, we divided the dynamical distribution $w_{\text{dyn}}(J, E_{\text{rot}}, E_{\text{vib}})$ by $2J + 1$, which is the leading factor of the old statistical weight. Then, we binned these 3D-data into a 2D-histogram in E_{tot} and E_{rot} in order to produce a smooth $(E_{\text{tot}}, E_{\text{rot}})$ -distribution. Next, each box of this histogram was divided by $\exp\{-E_{\text{tot}}/kT\}$, which is the remaining factor of the old statistical weight. Finally, the 2D-data of $(E_{\text{tot}}, E_{\text{rot}})$ -distribution were projected onto the axis $E_{\text{vib}} = E_{\text{tot}} - E_{\text{rot}}$, which gave smooth one-dimensional reweighting function $w_{\text{dyn}}(E_{\text{vib}})$. Multiplication of the statistical third-order rate constant $\kappa^{(n)}$ for a given vibrational state n at energy E_{vib} by the reweighting function $w_{\text{dyn}}(E_{\text{vib}})$ converts $\kappa^{(n)}$ it into a *dynamical* rate constant.

Such *dynamical* versions of third-order rate constants $\kappa^{(n)}$ are also given in Table II and represent the final result of this paper. We see that the values of dynamical $\kappa^{(n)}$ decrease as we go down the vibrational spectrum, but not as quickly as in the case of purely rotational version of $\kappa^{(n)}$. Ten upper vibrational states studied in this work are sufficient for computing a reasonably converged value of total κ . The result is $\kappa = 25.4 \times 10^{-35} \text{ cm}^6/\text{s}$, in good agreement with experimental value of κ^{ET} .

E. Energy transfer functions

In Figure 7 we present the energy transfer functions for three initial vibrational states: 41, 45, and 51. These functions are typical and allow demonstrating all properties of the energy transfer in this system. For each state we show two functions: $\bar{\sigma}_{n,\text{tran}}$ and $\bar{\sigma}_{n,\text{stab}}$. The function $\bar{\sigma}_{n,\text{tran}}$ includes all channels of the vibrational energy transfer (up, down, and elastic), while $\bar{\sigma}_{n,\text{stab}}$ includes only the vibrational stabilization (down). We see clearly that the total energy transfer is

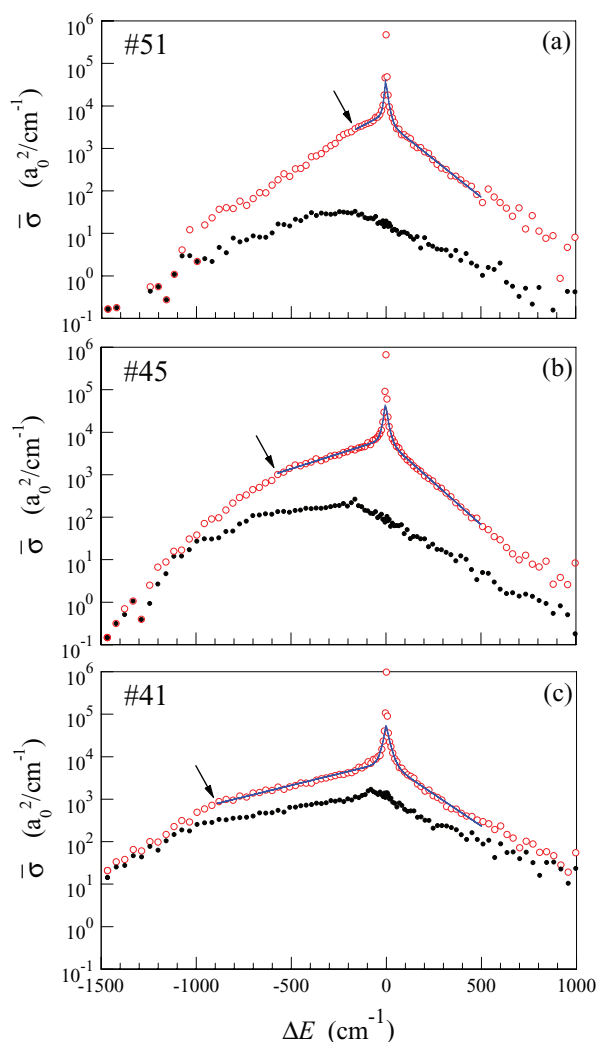


FIG. 7. Energy transfer functions $\bar{\sigma}_{n,\text{stab}}$ (black dots) and $\bar{\sigma}_{n,\text{tran}}$ (red circles) for three initial vibrational states: (a) $n = 51$; (b) $n = 45$; and (c) $n = 41$. Blue curves show the fit of each shoulder of $\bar{\sigma}_{n,\text{tran}}$ by a double exponential model. Arrow indicates the drop-off point.

characterized by a very pronounced elastic peak (note the log scale in Fig. 7), which is a well known artifact of all classical trajectory simulations. Although the value of $\bar{\sigma}_{n,\text{tran}}$ is, strictly speaking, divergent at the elastic peak, in the vicinity of the elastic peak it is usual to fit the energy transfer data by a double-exponential model, Eq. (32). We carried out such fitting for all initial vibrational states studied here. Results are summarized in Table IV, separately for the left ($\Delta E < 0$, de-excitation) and right ($\Delta E > 0$, excitation) shoulders of the energy transfer functions.

The width of elastic peak is characterized by the value of parameter γ in the first exponent of Eq. (32). Analysis of γ -values for excitation vs. de-excitation processes (right vs. left shoulders) shows that for all initial vibrational states the elastic peak is nearly symmetric. This is also seen in Fig. 7 and is consistent with understanding that the overall energy transfer due to elastic scattering should vanish. Analysis of γ -values for different initial vibrational states shows that the elastic peak flattens out as energy of the vibrational state decreases. Using the data of Tables II and IV we plotted the dependence of γ on the vibrational energy of the initial state and found that this dependence is linear. (Not shown here. If interested, readers can easily plot the data of Column 3 in Table IV vs. those of Column 2 in Table II). Explanation of this flattening is that for the lower vibrational states, where the rotational energy is higher, the rotational energy transfer is more efficient.

Apart from the elastic peak, the shape of the most important part of the energy transfer function is characterized by the value of parameter d in the second exponent of Eq. (32). We found that for all vibrational states considered here the de-excitation shoulder is considerably flatter than the excitation shoulder (see Fig. 7). Thus, the value of $\bar{\sigma}_{n,\text{tran}}$ in the excitation region drops faster, which means that de-excitation is more efficient than excitation. Thus, the overall effect of the energy transfer is de-excitation, which is consistent with expectation that the stable ozone is formed in the $\text{O}_3^* + \text{Ar}$ collisions. Again, we found that slopes of both excitation and de-excitation shoulders decrease as we go down the vibrational spectrum (see Table IV and Fig. 7). The dependence of d on the initial vibrational energy is also roughly linear.

One more property of $\bar{\sigma}_{n,\text{tran}}$ is worth noting. Figures 7(a)–7(c) show that the excitation shoulder is always represented well by the second exponential function (d -parameter) in a very broad range of ΔE . However, we found that each de-excitation shoulder exhibits a very clear drop-off, so that the value of d -parameter is meaningful only in the range between the drop-off point and the elastic peak (see Fig. 7). We also found that position of the drop-off depends on the initial vibrational state and moves to larger negative values of ΔE as we go down the vibrational spectrum. For example, for three states 51, 45, and 41, shown in Fig. 7 the drop-off point occurs close to $\Delta E = -240 \text{ cm}^{-1}$, -570 cm^{-1} , and -955 cm^{-1} , respectively. Analysis shows that these values correlate with rotational energy needed to lift the vibrational states above the dissociation threshold (which is also the value of vibrational energy below the threshold, see Table II). During the energy transfer, the *rotational* energy is transferred from O_3^* to Ar very efficiently and the slope of

TABLE IV. Parameters of the energy transfer functions.

Initial state	Analytic fit (de-excitation)				Analytic fit (excitation)				Numeric ^a			Inelastic
	$\bar{\sigma}_{n,\text{tran}}(0)$ $10^3 \frac{a_0^2}{\text{cm}^{-1}}$	γ (cm^{-1})	d (cm^{-1})	c	$\bar{\sigma}_{n,\text{tran}}(0)$ $10^3 \frac{a_0^2}{\text{cm}^{-1}}$	γ (cm^{-1})	d (cm^{-1})	c	$\langle \Delta E_{\downarrow} \rangle$ (cm^{-1})	$\langle \Delta E_{\uparrow} \rangle$ (cm^{-1})	$\langle \Delta E \rangle$ (cm^{-1})	$\langle \Delta E \rangle$ (cm^{-1})
51	45.65	7.39	186.65	0.147	29.22	11.81	121.81	0.149	-124.16	80.59	-44.30	-241.76
49, 50	47.27	11.19	322.70	0.117	38.34	8.17	79.74	0.130	-126.76	51.79	-78.78	-193.47
48	50.78	9.10	278.60	0.127	43.62	11.21	119.05	0.127	-164.28	79.40	-73.94	-177.89
46, 47	60.19	11.00	273.12	0.127	39.08	10.92	92.42	0.160	-146.78	57.68	-86.86	-133.61
45	51.82	11.16	305.21	0.136	33.07	12.77	109.20	0.198	-180.37	73.07	-100.51	-142.03
44	57.28	15.78	346.64	0.155	47.78	15.16	130.76	0.160	-205.58	81.63	-114.55	-250.65
43	64.40	14.55	356.26	0.144	50.67	15.61	128.08	0.165	-211.66	80.86	-118.52	-209.63
41, 42	53.45	14.89	397.36	0.140	43.91	18.24	144.57	0.168	-247.85	103.01	-124.63	-251.00
39, 40	33.46	21.16	415.46	0.179	35.04	20.53	142.61	0.191	-254.85	99.88	-126.61	-168.42
38	39.63	22.28	467.50	0.190	51.04	24.43	147.58	0.178	-292.17	140.20	-121.97	-197.70

^aTrajectories with $|\Delta E| < 3 \text{ cm}^{-1}$ and $|\Delta J| < 0.2$ were disregarded.

the de-excitation shoulder is defined mostly by this process. When the transferred energy is small (ΔE is close to the elastic peak) all the rotational states of the (J, K) -distribution are contributing to the process. The drop-off point is observed when the lower scattering resonances (those at the bound states border, see Fig. 2) stop contributing, simply because they do not have enough rotational energy to give. As we pass the drop-off point and go further down into the region of larger negative ΔE , fewer and fewer rotational states are able to contribute, rendering the overall energy transfer less and less efficient, and causing the value of $\bar{\sigma}_{n,\text{tran}}$ function to drop faster. This effect explains occurrence of the drop-off point in Fig. 7.

The functions $\bar{\sigma}_{n,\text{stab}}$ (for the vibrational energy transfer down) are also shown on each frame of Fig. 7. Their most important feature is absence of the elastic peak. Note that removing the elastic peak rigorously is an unresolved and well-known deficiency of all classical trajectory simulations. In our mixed quantum-classical method the elastic peak can be removed easily and rigorously. Similar to $\bar{\sigma}_{n,\text{tran}}$, the shapes of all $\bar{\sigma}_{n,\text{stab}}$ dependencies are characterized by the following three properties: (1) excitation and de-excitation shoulders both are well described by single-exponential functions; (2) de-excitation shoulder is flatter than the excitation shoulder; (3) de-excitation shoulder exhibits the drop-off point. We did not fit the $\bar{\sigma}_{n,\text{stab}}$ functions by analytic expressions, but we checked that, according to Eq. (31), integrating the $\bar{\sigma}_{n,\text{stab}}$ functions recovers the values of $\kappa^{(n)}$ given in Table II.

Finally, comparison of $\bar{\sigma}_{n,\text{stab}}$ vs. $\bar{\sigma}_{n,\text{tran}}$ in Figs. 7(a)–7(c) shows that in the vicinity of the elastic peak the magnitude of $\bar{\sigma}_{n,\text{stab}}$ is, usually, one or two orders of magnitude smaller than the magnitude of the overall $\bar{\sigma}_{n,\text{tran}}$. This is expected because, when the amount of transferred energy is relatively small (say $\Delta E \leq kT$), the rotational energy transfer plays the dominant role. However, one should remember that the vibrational energy transfer becomes essential in the $\Delta E \gg kT$ regime, when the internal rotational energy of O_3^* by itself is simply insufficient. It is important to stress that this vibrationally inelastic energy transfer is responsible for

quenching of the scattering resonances O_3^* into the stable O_3 states.

Some of the data presented in this section can be compared to results of the previous work. For example, the energy transfer function for $\text{O}_3^* + \text{Ar}$ collisions, determined from the classical trajectory simulations, has been reported earlier in Ref. 37 and has been further analyzed in Ref. 63. Using the actual data of Ref. 37 for $T = 298 \text{ K}$, we have fitted their energy transfer function (see Fig. 2(a) in Ref. 37) by the double exponential model, Eq. (32). This gave us $\gamma = 11.1 \text{ cm}^{-1}$ and $d = 153.8 \text{ cm}^{-1}$ for the de-excitation process, and $\gamma = 7.9 \text{ cm}^{-1}$ and $d = 93.0 \text{ cm}^{-1}$ for the excitation process. These data compare favorably to the fit of the energy transfer function obtained in this work for the upper vibrational state (state 51, see Table IV). The differences of slopes are on the order of 30% for the vicinity of the elastic peak (γ) and are on the order of 15% for the wings (d). One should not really expect better agreement for the following reason – the internal ro-vibrational energies are somewhat different in the two calculations we are trying to compare. Namely, the classical trajectory simulations in Ref. 37 are characterized by the energy distribution presented in Fig. 6 (peaked at $E_{\text{vib}} = -50 \text{ cm}^{-1}$), while in this work the initial vibrational energy is considerably lower and is quantized. Even the upper vibrational state, 51, is characterized by $E_{\text{vib}} = -238.2 \text{ cm}^{-1}$. This means that in our calculations for state 51 the rotational excitation is higher, compared to the classical model of Ref. 37, by almost 190 cm^{-1} . The other (lower vibrational energy) states studied here possess even higher rotational energies, and we clearly observe the tendency to more efficient energy transfer in such calculations, compared to results of the Ref. 37 (see data for other states in Table IV).

We have also computed the average values of energy transfer to compare with results of the classical trajectory simulations in Ref. 37. Those results at $T = 298 \text{ K}$ are: $\langle \Delta E_{\uparrow} \rangle = 79.24 \text{ cm}^{-1}$, $\langle \Delta E_{\downarrow} \rangle = -134.33 \text{ cm}^{-1}$, and $\langle \Delta E \rangle = -43.61 \text{ cm}^{-1}$ (see Table I in Ref. 37). We tried to analyze our data in the way identical to that of Ref. 37, by keeping the elastic channel, $n' = n$, and removing the

elastic peak manually (by disregarding trajectories with $|\Delta E| < 3 \text{ cm}^{-1}$ and $|\Delta J| < 0.2$). For the upper state, 51, we obtained: $\langle \Delta E_{\uparrow} \rangle = 80.59 \text{ cm}^{-1}$, $\langle \Delta E_{\downarrow} \rangle = -124.16 \text{ cm}^{-1}$, and $\langle \Delta E \rangle = -44.30 \text{ cm}^{-1}$, in very good agreement with results of Ref. 37. We also found that as we go down the vibrational spectrum (to higher levels of rotational excitation) the values of energy transfer increase quite substantially (see Table IV). This behavior is consistent with effect of the initial rotational energy discussed in the previous paragraph.

We decided not to conduct comparison of our results with results of Refs. 38 and 39, because those were obtained for quenching of the bound states of non-rotating O_3 ($J = 0$), quite different from what is studied here (metastable O_3^* with up to $J \sim 90$). Indeed, in the light of discussion above, such comparison would not be particularly meaningful, since the magnitude of the initial rotational excitation has essential influence on the energy transfer. In principle, we could generate the $J = 0$ data using the mixed quantum-classical theory, but we decided that this would not be particularly instructive.

Another paper to compare with is the work of Troe and co-workers,⁴⁷ where analysis of the experimental information led to the value of $\langle \Delta E \rangle = -20 \pm 10 \text{ cm}^{-1}$. Note that analysis of Troe incorporates a single exponential model for the energy transfer function. Our results, as well as classical trajectory results,³⁷ indicate very clearly that the energy transfer is double-exponential (see Table IV and Fig. 7). Thus, it is not clear what slopes should be used for comparison to the data of Troe, and whether such comparison is meaningful. For example, in our calculations the elastic peak is almost symmetric (the values of γ for excitation and de-excitation are very similar), leading to the resultant value of roughly $\langle \Delta E \rangle \sim 0$. The difference of slopes at the wings (values of d for excitation and de-excitation) gives for the upper state, 51: $\langle \Delta E \rangle = -65 \text{ cm}^{-1}$. All we can say is that both the value of Troe, $\langle \Delta E \rangle = -20 \pm 10 \text{ cm}^{-1}$, and the average energy transfer we computed here for the upper state, $\langle \Delta E \rangle = -44.30 \text{ cm}^{-1}$, are inside of this interval: $0 < \langle \Delta E \rangle < -65 \text{ cm}^{-1}$.

Finally, in his empirical statistical model of the energy transfer,²⁶ Marcus used the value of $\langle \Delta E_{\downarrow} \rangle = -210 \text{ cm}^{-1}$. This number is much larger than the value we obtained here for the upper vibrational state, $\langle \Delta E_{\downarrow} \rangle = -124.16 \text{ cm}^{-1}$. Note, however, that lower vibrational states (excited rotationally) demonstrate larger values of $\langle \Delta E_{\downarrow} \rangle$ (see Table IV). For example, state 44 exhibits the value of $\langle \Delta E_{\downarrow} \rangle = -205.58 \text{ cm}^{-1}$, very close to Marcus's value. Recall that this particular state has dominant contribution to the process (the largest stabilization cross section, see Tables I and II), which may finally be an explanation of seemingly unreasonable (unexpectedly large) value obtained by Marcus trying to fit the experiment.

Also, we feel that most of uncertainty in the calculations of average energy transfer comes from some arbitrariness in the treatment of the elastic peak. We can easily avoid this uncertainty by calculating the energy transfer through the vibrationally inelastic channels only, $n' \neq n$. For completeness, these data are presented in the last column of Table IV. As one might expect, the values of average energy transfer computed

in this way are higher, compared to those computed with inclusion of the sharp elastic peak.

V. CONCLUSIONS

Let us summarize major achievements and findings of this work. First of all, we formulated a general theoretical basis for efficient use of the mixed quantum-classical method in calculations of the rate constant of recombination reaction that proceeds according to the energy transfer mechanism. Efficiency of our approach is achieved by simultaneous weighted sampling of several quasi-classical parameters of the system: impact parameter of the quencher, its incident direction, thermal energy of the molecule + quencher collisions and, finally, the distribution of initial rotational states of the energized molecule. The procedure is general and can be applied to many processes relevant to combustion,⁶⁶ astrochemistry,⁶⁷ and atmospheric chemistry.⁶⁸

Second, we applied this method to address a long-standing problem – the recombination reaction that forms ozone. We computed the rotationally averaged cross sections for vibrational state-to-state transitions in the process of quenching the metastable O_3^* by collisions with thermal Ar bath at room temperature. Major properties of the state-to-state cross sections for scattering resonances that correlate with ten upper vibrational states of ozone were discussed and explained in quantum mechanical terms, such as shapes of vibrational wave functions and energy separation of quantized states. This information was further used to obtain the third-order thermal rate constant for the recombination reaction that forms ozone. The energy transfer functions were derived, separately for each participating scattering resonance.

Third, based on analysis of additional quasi-classical trajectory simulations, we found that dynamic effects are absolutely essential in determining the distribution of ro-vibrational scattering resonances that participate in the process of ozone formation. In such situation the ergodic hypothesis fails miserably and the usual statistical treatment is inappropriate. Good agreement with experiment is obtained only when this dynamic information is included into the treatment. In fact, this result is not very surprising and could be considered as firm confirmation of the previous work, because several non-statistical features of the ozone molecule itself and of the ozone forming reaction have already been reported by others.⁵¹⁻⁵⁴

Concerning comparison of our theoretical results against experimental results: The value of third order recombination rate constant obtained here is $\kappa = 25.4 \times 10^{-35} \text{ cm}^6/\text{s}$, astonishingly close to the experimental rate of $\kappa^{\text{ET}} = 24.8 \times 10^{-35} \text{ cm}^6/\text{s}$. Although it is very tempting to say that the agreement is excellent, we should admit that it is most probably accidental. We do not use any adjustable parameters in our model, but we use several simplifying assumptions that normally are expected to affect the predicted recombination rate. The major assumption is, certainly, the adiabatic treatment of bending. Rough estimates carried out during the review stage of this work showed that the bending mode in ozone is probably as important as the other two modes. This may mean that the predicted recombination rate coefficient is

underestimated by 50% or so. Note, however, that the way in which the experimental value is derived also carries a significant degree of uncertainty, particularly in the splitting of the overall reaction rate, $\kappa^{\text{exp}} = 65.3 \times 10^{-35} \text{ cm}^6/\text{s}$, onto contributions from the energy-transfer mechanism, κ^{ET} , and from the Chaperon mechanism. Thus, we would not make a big deal of the seemingly excellent agreement obtained here and just state that our model describes the recombination process adequately.

We believe that this work represents an important milestone in the theoretical research on the recombination reaction that forms ozone. Over the past 10 years of active research on ozone, the first step of the ozone forming reaction, Eq. (4), has received the most of attention. Thus, the importance of the ΔZPE -effect in the $\text{O} + \text{O}_2 \leftrightarrow \text{O}_3^*$ process⁶⁹ has been recognized by all authors working on this topic and has been introduced into the statistical,^{25–28} quantum,^{18–24,32} and even into the classical trajectory³⁰ theories of the process. In contrast, very limited progress has been made on modeling the second step of the ozone forming reaction, Eq. (5). This is quite unfortunate, since it is expected that this very process, $\text{O}_3^* + \text{M} \rightarrow \text{O}_3 + \text{M}$, gives rise to the so called η -effect,^{25–28} originating in the quantum symmetry and leading to the famous anomalous isotope enrichments observed in the stratospheric ozone. The attempts of theorists to put a rigorous basis under the η -effect have not been successful so far. The methods used to treat the energy transfer step were either purely classical^{36,37} (where the quantum symmetry cannot be reproduced in principle) or approximate quantum mechanical, biased to the $J = 0$ model of non-rotating O_3^* ,^{33–35,38,39} which also cannot be reliable due to large rotational excitation of O_3^* and a very distinct rotational dynamics of the $\text{O}_3^* + \text{M}$ collisions. The importance of this paper is that, finally, an approach is devised for treatment of the energy transfer step, which incorporates quantum mechanics for the vibrational state-to-state transitions in O_3^* , but also includes a reasonable description of its rotational dynamics, by means of the classical trajectories. Our method is still approximate, but we view it as an affordable middle between the quantum and classical approaches to this problem. Here we demonstrate that our method gives good agreement with experiment and allows gaining very detailed unique insight into the vibrational quenching of rotationally excited O_3^* (up to $J \sim 90$). Within this approach, we should be able to study the temperature dependence of the recombination rate (in a broad range of temperatures) and the quenching of O_3^* by molecules typical to Earth's atmosphere (e.g., $\text{M} = \text{N}_2$). Another open question is molecular origin of the η -effect.

Based on what we have learned in this work the following further improvement of the ozone treatment is clearly seen. Instead of sampling the initial rotational states (separately for each vibrational state) using the analytic statistical distribution of Eq. (14), one could sample the initial ro-vibrational states of scattering resonances directly from the dynamic O_3^* distribution $w_{\text{dyn}}(J, K, E_{\text{vib}})$ presented in Fig. 6. From the computational point of view, such calculations of the reaction rate constant would be most economic, although the detailed insight into the mechanisms of state-to-state transitions (presented in this paper) would probably be missing.

It is also desirable to incorporate more accurate O_3 PES into the dynamics calculations. Two new potential energy surfaces for ozone have been recently developed^{70,71} with focus on reproducing correctly the dissociation energy of O_3 , and the behavior near the “reef” along the minimum energy path. Presence of the “reef” is known to affect the temperature dependence of the atom exchange reaction (e.g., $^{16}\text{O} + ^{18}\text{O}^{16}\text{O} \rightarrow ^{16}\text{O}^{18}\text{O} + ^{16}\text{O}$), and may also affect the recombination process. This question also remains open.

ACKNOWLEDGMENTS

This research was supported by the NSF Atmospheric Chemistry Program, Division of Atmospheric Sciences, Grant No. 0842530. This research used resources of the National Energy Research Scientific Computing Center, which is supported by the Office of Science of the U.S. Department of Energy (DOE) (Contract No. DE-AC02-05CH11231).

- ¹A. W. Jasper and J. A. Miller, *J. Phys. Chem. A* **113**, 5612 (2009).
- ²R. X. Fernandes, K. Luther, J. Troe, and V. G. Ushakov, *Phys. Chem. Chem. Phys.* **10**, 4313 (2008).
- ³V. Bernshtein and I. Oref, *Isr. J. Chem.* **47**, 205 (2008).
- ⁴W. Miller, *Faraday Discuss.* **102**, 53 (1995).
- ⁵G. S. Whittier and J. C. Light, *J. Chem. Phys.* **110**, 4280 (1999).
- ⁶D. H. Zhang and J. C. Light, *J. Chem. Phys.* **105**, 1291 (1996).
- ⁷D. M. Medvedev, S. K. Gray, E. M. Goldfield, M. J. Lakin, D. Troya, and G. C. Schatz, *J. Chem. Phys.* **120**, 1231 (2004).
- ⁸S. Zhang, D. M. Medvedev, E. M. Goldfield, and S. K. Gray, *J. Chem. Phys.* **125**, 164312 (2006).
- ⁹D. H. Zhang, *J. Chem. Phys.* **125**, 133102 (2006).
- ¹⁰Y. Lu, S.-Y. Lee, and D. H. Zhang, *J. Chem. Phys.* **124**, 011101 (2006).
- ¹¹A. Kuppermann, *J. Phys. Chem.* **108**, 8894 (2004).
- ¹²M. V. Ivanov and D. Babikov, *J. Chem. Phys.* **134**, 144107 (2011).
- ¹³J. M. Bowman, *Chem. Phys. Lett.* **217**, 36 (1994).
- ¹⁴J. Qi and J. M. Bowman, *J. Chem. Phys.* **105**, 9884 (1996).
- ¹⁵J. Qi and J. M. Bowman, *J. Chem. Phys.* **107**, 9960 (1997).
- ¹⁶M. V. Ivanov and D. Babikov, *J. Chem. Phys.* **134**, 174308 (2011).
- ¹⁷J. Troe, *J. Chem. Phys.* **66**, 4745 (1977).
- ¹⁸D. Babikov, B. Kendrick, R. B. Walker, R. Schinke, and R. T. Pack, *Chem. Phys. Lett.* **372**, 686 (2003).
- ¹⁹D. Babikov, B. Kendrick, R. B. Walker, R. T. Pack, P. Fleurat-Lessard, and R. Schinke, *J. Chem. Phys.* **118**, 6298 (2003).
- ²⁰D. Babikov, B. Kendrick, R. B. Walker, and R. T. Pack, *J. Chem. Phys.* **119**, 2577 (2003).
- ²¹E. Vetoshkin and D. Babikov, *J. Chem. Phys.* **125**, 24302 (2006).
- ²²E. Vetoshkin and D. Babikov, *J. Chem. Phys.* **127**, 154312 (2007).
- ²³E. Vetoshkin and D. Babikov, *Phys. Rev. Lett.* **99**, 138301 (2007).
- ²⁴L. Jiang and D. Babikov, *Chem. Phys. Lett.* **474**, 273 (2009).
- ²⁵Y. Q. Gao and R. A. Marcus, *Science* **293**, 259 (2001); see also technical comment C. Janssen and R. A. Marcus, *ibid.* **294**, 951a (2001).
- ²⁶Y. Q. Gao and R. A. Marcus, *J. Chem. Phys.* **116**, 137 (2002).
- ²⁷Y. Q. Gao, W.-C. Chen, and R. A. Marcus, *J. Chem. Phys.* **117**, 1536 (2002).
- ²⁸Y. Q. Gao and R. A. Marcus, *J. Chem. Phys.* **127**, 244316 (2007).
- ²⁹P. Fleurat-Lessard, S. Y. Grebenshchikov, R. Schinke, C. Janssen, and D. Krankowsky, *J. Chem. Phys.* **119**, 4700 (2003).
- ³⁰R. Schinke and P. Fleurat-Lessard, *J. Chem. Phys.* **122**, 094317 (2005).
- ³¹R. Schinke, S. Y. Grebenshchikov, M. V. Ivanov, and P. Fleurat-Lessard, *Annu. Rev. Phys. Chem.* **625** (2006).
- ³²S. Y. Grebenshchikov and R. Schinke, *J. Chem. Phys.* **131**, 181103 (2009).
- ³³D. Charlo and D. C. Clary, *J. Chem. Phys.* **117**, 1660 (2002).
- ³⁴D. Charlo and D. C. Clary, *J. Chem. Phys.* **120**, 2700 (2004).
- ³⁵T. Xie and J. M. Bowman, *Chem. Phys. Lett.* **412**, 131 (2005).
- ³⁶M. V. Ivanov, S. Y. Grebenshchikov, and R. Schinke, *J. Chem. Phys.* **120**, 10015 (2004).
- ³⁷M. V. Ivanov and R. Schinke, *J. Chem. Phys.* **122**, 234318 (2005).

- ³⁸M. V. Ivanov, S. Y. Grebenshchikov, and R. Schinke, *J. Chem. Phys.* **130**, 174311 (2009).
- ³⁹M. V. Ivanov and R. Schinke, *Mol. Phys.* **108**, 259 (2010).
- ⁴⁰R. T Pack, R. B. Walker, and B. K. Kendrick, *J. Chem. Phys.* **109**, 6701 (1998).
- ⁴¹R. T Pack, R. B. Walker, and B. K. Kendrick, *J. Chem. Phys.* **109**, 6714 (1998).
- ⁴²R. T Pack and R. B. Walker, *J. Chem. Phys.* **121**, 800 (2004).
- ⁴³D. Babikov, *J. Chem. Phys.* **119**, 6554 (2003).
- ⁴⁴S. Y. Grebenshchikov, R. Schinke, P. Fleurat-Lessard, and M. Joyeux, *J. Chem. Phys.* **119**, 6512 (2003).
- ⁴⁵H.-S. Lee and J. C. Light, *J. Chem. Phys.* **120**, 5859 (2004).
- ⁴⁶K. Luther, K. Oum, and J. Troe, *Phys. Chem. Chem. Phys.* **7**, 2764 (2005).
- ⁴⁷H. Hippler, R. Rahn, and J. Troe, *J. Chem. Phys.* **93**, 6560 (1990).
- ⁴⁸G. H. Peslherbe, H. Wang, and W. L. Hase, *J. Chem. Phys.* **102**, 5626 (1995).
- ⁴⁹J. Mikosch, R. Otto, S. Trippel, C. Eichhorn, M. Weidemu"ller, and R. Wester, *J. Phys. Chem. A* **112**, 10448 (2008).
- ⁵⁰R. A. Marcus, William L. Hase, and Kandadai Swamy, *J. Phys. Chem.* **88**, 6717 (1984).
- ⁵¹S. C. Farantos, R. Schinke, H. Guo, and M. Joyeux, *Chem. Rev.* **109**, 4248 (2009).
- ⁵²R. Siebert, P. Fleurat-Lessard, R. Schinke, M. Bittererova, and S. C. Farantos, *J. Chem. Phys.* **116**, 9749 (2002).
- ⁵³M. Kryvohuz and R. A. Marcus, *J. Chem. Phys.* **132**, 224304 (2010).
- ⁵⁴A. L. van Wyngarden, K. A. Mar, K. A. Boering, J. J. Lin, Y. T. Lee, S.-Y. Lin, H. Guo, and G. Lendvay, *J. Am. Chem. Soc.* **129**, 2866 (2007).
- ⁵⁵G. H. Peslherbe, H. Wang, and W. L. Hase, *Adv. Chem. Phys.* **105**, 171 (1999).
- ⁵⁶G. Herzberg, *Infrared and Raman Spectra of Polyatomic Molecules* (Van Nostrand, Princeton, 1945).
- ⁵⁷N. J. Brown and J. A. Miller, *J. Chem. Phys.* **80**, 5568 (1984).
- ⁵⁸E. T. Sevy, S. M. Rubin, Z. Lin, and G. W. Flynn, *J. Chem. Phys.* **113**, 4912 (2000).
- ⁵⁹G. Lendvay and G. Schatz, *J. Phys. Chem.* **96**, 3753 (1992).
- ⁶⁰G. Lendvay and G. Schatz, *J. Phys. Chem.* **98**, 6530 (1994).
- ⁶¹I. Oref and D. C. Tardy, *Chem. Rev.* **90**, 1407 (1990).
- ⁶²J. Troe and M. Quack, *Gas Kinetics and Energy Transfer, Specialist Periodical Report* (Chemical Society, Burlington House, London, 1977), Vol. 2.
- ⁶³Z. Zhu and R. A. Marcus, *J. Chem. Phys.* **129**, 214106 (2008).
- ⁶⁴S. M. Anderson, D. Hülsebusch, and K. Mauersberger, *J. Chem. Phys.* **107**, 5385 (1997).
- ⁶⁵C. Janssen, J. Guenther, D. Krankowsky, and C. Mauersberger, *J. Chem. Phys.* **111**, 7179 (1999).
- ⁶⁶D. K. Havey, J. Du, and A. S. Mullin, *J. Phys. Chem. A* **114**, 1569 (2010).
- ⁶⁷A. Faure, L. Wiesenfeld, M. Wernli, and P. Valiron, *J. Chem. Phys.* **123**, 104309 (2005).
- ⁶⁸L. P. Dempsey, T. D. Sechler, C. Murray, and M. I. Lester, *J. Phys. Chem. A* **113**, 6851 (2009).
- ⁶⁹C. Janssen, J. Guenther, K. Mauersberger, and D. Krankowsky, *Phys. Chem. Chem. Phys.* **3**, 4718 (2001).
- ⁷⁰R. Dawes, P. Lolur, J. Ma, and H. Guo, *J. Chem. Phys.* **135**, 081102 (2011).
- ⁷¹M. Ayouz and D. Babikov, *Adv. Phys. Chem.* **2012**, 951371 (2012).